

Euclid: The search for primordial features[★]

M. Ballardini^{1,2,3,★}, Y. Akrami^{4,5}, F. Finelli^{3,6}, D. Karagiannis⁷, B. Li⁸, Y. Li⁹, Z. Sakr^{10,11,12}, D. Sapone¹³,
 A. Achúcarro^{14,15}, M. Baldi^{16,3,17}, N. Bartolo^{18,19,20}, G. Cañas-Herrera^{21,14}, S. Casas²², R. Murgia^{23,24},
 H.-A. Winther²⁵, M. Viel^{26,27,28,29}, A. Andrews³, J. Jasche^{30,31}, G. Lavaux³², D. K. Hazra^{3,33,34}, D. Paoletti^{3,6},
 J. Valiviita^{35,36}, A. Amara³⁷, S. Andreon³⁸, N. Auricchio³, P. Battaglia³, D. Bonino³⁹, E. Branchini^{40,41},
 M. Brescia^{42,43,44}, J. Brinchmann⁴⁵, S. Camera^{46,47,39}, V. Capobianco³⁹, C. Carbone⁴⁸, J. Carretero^{49,50},
 M. Castellano⁵¹, S. Cavuoti^{43,44}, A. Cimatti⁵², G. Congedo⁵³, L. Conversi^{54,55}, Y. Copin⁵⁶, L. Corcione³⁹, F. Courbin⁵⁷,
 H. M. Courtois⁵⁸, A. Da Silva^{59,60}, H. Degaudenzi⁶¹, F. Dubath⁶¹, X. Dupac⁵⁵, M. Farina⁶², S. Farrens⁶³, M. Frailis²⁷,
 E. Franceschi³, M. Fumana⁴⁸, S. Galeotta²⁷, B. Gillis⁵³, C. Giocoli^{3,17}, A. Grazian²⁰, F. Grupp^{64,65}, S. V. H. Haugan²⁵,
 W. Holmes⁶⁶, F. Hormuth⁶⁷, A. Hornstrup^{68,69}, P. Hudelot³², K. Jahnke⁷⁰, S. Kermiche⁷¹, A. Kiessling⁶⁶, M. Kunz⁷²,
 H. Kurki-Suonio^{35,36}, P. B. Lilje²⁵, V. Lindholm^{35,36}, I. Lloro⁷³, E. Maiorano³, O. Mansutti²⁷, O. Marggraf⁷⁴,
 N. Martinet⁷⁵, F. Marulli^{76,3,17}, R. Massey⁸, E. Medinaceli³, S. Mei⁷⁷, Y. Mellier^{31,32}, M. Meneghetti^{3,17}, E. Merlin⁵¹,
 G. Meylan⁵⁷, M. Moresco^{76,3}, L. Moscardini^{76,3,17}, E. Munari²⁷, S.-M. Niemi²¹, C. Padilla⁴⁹, S. Paltani⁶¹, F. Pasian²⁷,
 K. Pedersen⁷⁸, W. J. Percival^{79,80,81}, V. Pettorino⁸², S. Pires⁶³, G. Polenta⁸³, M. Poncet⁸⁴, L. A. Popa⁸⁵, L. Pozzetti³,
 F. Raison⁶⁴, A. Renzi^{18,19}, J. Rhodes⁶⁶, G. Riccio⁴³, E. Romelli²⁷, M. Roncarelli³, R. Saglia^{86,64}, B. Sartoris^{86,27},
 T. Schrabback⁸⁷, A. Secroun⁷¹, G. Seidel⁷⁰, S. Serrano^{88,89,90}, C. Sirignano^{18,19}, G. Sirri¹⁷, L. Stanco¹⁹, J.-L. Starck⁹¹,
 C. Surace⁷⁵, P. Tallada-Crespi^{92,50}, A. N. Taylor⁵³, I. Tereno^{59,93}, R. Toledo-Moreo⁹⁴, F. Torradeflot^{50,92}, I. Tutusaus¹¹,
 E. A. Valentijn⁹⁵, L. Valenziano^{3,6}, T. Vassallo^{86,27}, A. Veropalumbo^{38,41}, Y. Wang⁹⁶, J. Weller^{86,64}, G. Zamorani³,
 J. Zoubian⁷¹, V. Scottez^{31,97}

(Affiliations can be found after the references)

April 1, 2024

ABSTRACT

Primordial features, in particular oscillatory signals, imprinted in the primordial power spectrum of density perturbations represent a clear window of opportunity for detecting new physics at high-energy scales. Future spectroscopic and photometric measurements from the *Euclid* space mission will provide unique constraints on the primordial power spectrum, thanks to the redshift coverage and high-accuracy measurement of nonlinear scales, thus allowing us to investigate deviations from the standard power-law primordial power spectrum. We consider two models with primordial undamped oscillations superimposed on the matter power spectrum described by $1 + \mathcal{A}_X \sin(\omega_X \Xi_X + 2\pi\phi_X)$, one linearly spaced in k space with $\Xi_{\text{lin}} \equiv k/k_*$ where $k_* = 0.05 \text{ Mpc}^{-1}$ and the other logarithmically spaced in k space with $\Xi_{\text{log}} \equiv \ln(k/k_*)$. We note that \mathcal{A}_X is the amplitude of the primordial feature, ω_X is the dimensionless frequency, and ϕ_X is the normalised phase, where $X = \{\text{lin}, \text{log}\}$. We provide forecasts from spectroscopic and photometric primary *Euclid* probes on the standard cosmological parameters $\Omega_{\text{m},0}$, $\Omega_{\text{b},0}$, h , n_s , and σ_8 , and the primordial feature parameters \mathcal{A}_X , ω_X , and ϕ_X . We focus on the uncertainties of the primordial feature amplitude \mathcal{A}_X and on the capability of *Euclid* to detect primordial features at a given frequency. We also study a nonlinear density reconstruction method in order to retrieve the oscillatory signals in the primordial power spectrum, which are damped on small scales in the late-time Universe due to cosmic structure formation. Finally, we also include the expected measurements from *Euclid*'s galaxy-clustering bispectrum and from observations of the cosmic microwave background (CMB). We forecast uncertainties in estimated values of the cosmological parameters with a Fisher matrix method applied to spectroscopic galaxy clustering (GC_{sp}), weak lensing (WL), photometric galaxy clustering (GC_{ph}), the cross correlation (XC) between GC_{ph} and WL, the spectroscopic galaxy clustering bispectrum, the CMB temperature and E -mode polarisation, the temperature-polarisation cross correlation, and CMB weak lensing. We consider two sets of specifications for the *Euclid* probes (pessimistic and optimistic) and three different CMB experiment configurations, that is, *Planck*, Simons Observatory (SO), and CMB Stage-4 (CMB-S4). We find the following percentage relative errors in the feature amplitude with *Euclid* primary probes: for the linear (logarithmic) feature model, with a fiducial value of $\mathcal{A}_X = 0.01$, $\omega_X = 10$, and $\phi_X = 0$: 21% (22%) in the pessimistic settings and 18% (18%) in the optimistic settings at a 68.3% confidence level (CL) using $\text{GC}_{\text{sp}} + \text{WL} + \text{GC}_{\text{ph}} + \text{XC}$. While the uncertainties on the feature amplitude are strongly dependent on the frequency value when single *Euclid* probes are considered, we find robust constraints on \mathcal{A}_X from the combination of spectroscopic and photometric measurements over the frequency range of $(1, 10^{2.1})$. Due to the inclusion of numerical reconstruction, the GC_{sp} bispectrum, SO-like CMB reduces the uncertainty on the primordial feature amplitude by 32%–48%, 50%–65%, and 15%–50%, respectively. Combining all the sources of information explored expected from *Euclid* in combination with the future SO-like CMB experiment, we forecast $\mathcal{A}_{\text{lin}} \simeq 0.010 \pm 0.001$ at a 68.3% CL and $\mathcal{A}_{\text{log}} \simeq 0.010 \pm 0.001$ for $\text{GC}_{\text{sp}}(\text{PS rec} + \text{BS}) + \text{WL} + \text{GC}_{\text{ph}} + \text{XC} + \text{SO-like}$ for both the optimistic and pessimistic settings over the frequency range $(1, 10^{2.1})$.

Key words. gravitation – gravitational lensing: weak – cosmological parameters – early Universe – large-scale structure of Universe

1. Introduction

Future galaxy surveys are the new frontier in the study of initial conditions of the Universe. They are expected to improve signif-

Article number, page 1 of 23

[★] This paper is published on behalf of the *Euclid* Consortium

^{**} e-mail: mario.ballardini@uni.fe.it

icantly the constraints on many of the parameters characterising the physics of the early Universe. The *Euclid* satellite, simultaneously performing a spectroscopic survey of galaxies and an imaging survey (targeting weak lensing and galaxy clustering using photometric redshifts), will have the unique opportunity of measuring ultra-large scales thanks to its large observed volume, as well as small scales of matter distribution in the full nonlinear regime. This opportunity will drastically improve our understanding of the early-Universe physics and of cosmic inflation (Starobinsky 1980; Guth 1981; Sato 1981; Linde 1982; Albrecht & Steinhardt 1982; Hawking et al. 1982; Linde 1983) through the study of the statistics hidden in the scalar density perturbations (Mukhanov & Chibisov 1981). *Euclid* measurements are indeed expected to reduce uncertainties on the amplitude of primordial scalar perturbations A_s , the scalar spectral index n_s and its derivatives (or scalar runnings), the amplitude of primordial non-Gaussianity f_{NL} (in particular of a local type), and the spatial curvature parameter Ω_K ; and to enable us to perform significantly more stringent tests of extended models beyond single-field slow-roll inflation (Laureijs et al. 2011; Amendola et al. 2018; Euclid Collaboration: Blanchard et al. 2020).

The goal of this paper is to summarise the status of, motivations for, and challenges in searching for oscillatory features in the primordial fluctuations (see Chluba et al. 2015; Achúcarro et al. 2022, for reviews) with large-scale structure (LSS) observations expected from *Euclid*. Searches for primordial features based on the cosmic microwave background (CMB) angular power spectra (Wang & Mathews 2002; Adams et al. 2001; Peiris et al. 2003; Mukherjee & Wang 2003; Covi et al. 2006; Hamann et al. 2007; Meerburg et al. 2012; Planck Collaboration: Ade et al. 2014b; Meerburg et al. 2014; Benetti 2013; Miranda & Hu 2014; Easther & Flauger 2014; Chen & Namjoo 2014; Achúcarro et al. 2014; Hazra et al. 2014a,b; Hu & Torrado 2015; Planck Collaboration: Ade et al. 2016b; Gruppuso & Sagnotti 2015; Gruppuso et al. 2016; Hazra et al. 2016; Torrado et al. 2017; Planck Collaboration: Akrami et al. 2020a; Zeng et al. 2019; Cañas-Herrera et al. 2021; Braglia et al. 2021, 2022b,a; Naik et al. 2022; Hamann & Wons 2022) and bispectra (Planck Collaboration: Ade et al. 2014a; Fergusson et al. 2015; Planck Collaboration: Ade et al. 2016a; Meerburg et al. 2016; Planck Collaboration: Akrami et al. 2020a,b) have so far not detected any statistically significant signal, setting constraints on deviations from a pure power-law primordial power spectrum (PPS) at the few percent level (depending on the methodology applied) for wavenumbers in the range $0.005 < k/(h \text{Mpc}^{-1}) < 0.2$. However, it is important to stress that there are interesting models of primordial features that are able to reproduce some of the anomalous features observed in the CMB temperature angular power spectrum at a marginal statistical significance of 99.7%. These include the dip in power in the multipole range $\ell \sim 20\text{--}40$ and an oscillatory pattern at the intermediate scales $\ell \sim 700\text{--}800$. Models with primordial features have also been studied in the context of the anomalous CMB lensing smoothing excess, as well as the H_0 and S_8 tensions (Planck Collaboration: Akrami et al. 2020a; Domènech & Kamionkowski 2019; Liu & Huang 2020; Domènech et al. 2020; Keeley et al. 2020; Hazra et al. 2022; Antony et al. 2023; Ballardini & Finelli 2022).

In the context of primordial features, large-volume photometric and spectroscopic surveys not only provide a complementary look at the structure on very large scales, but they can also provide a precise measurement of the power spectrum on small scales, complementing the CMB measurements and improving the sensitivity for high-frequency signals. This has been studied extensively with forecast analyses in Wang et al. (1999), Zhan

et al. (2006), Huang et al. (2012), Chen et al. (2016a), Chen et al. (2016b), Ballardini et al. (2016), Xu et al. (2016), Ansari Fard & Baghrani (2018), Palma et al. (2018), Ballardini et al. (2018), Ballardini (2019), Beutler et al. (2019), Ballardini et al. (2020), Debono et al. (2020), and Li et al. (2022) and demonstrated on real data in Beutler et al. (2019), Ballardini et al. (2023), and Mergulhão et al. (2023) showing that current galaxy clustering data of the Baryon Oscillation Spectroscopic Survey (BOSS) alone can already provide constraints that are competitive with those derived from the *Planck* CMB data. Given the potential of the *Euclid* mission, it is imperative to have a good description of the LSS observables on all observed scales, and to do so, nonlinear corrections need to be correctly accounted for (Vlah et al. 2016; Vasudevan et al. 2019; Beutler et al. 2019; Ballardini et al. 2020; Chen et al. 2020; Li et al. 2022; Ballardini & Finelli 2022).

In this paper, we forecast how well the surveys from the *Euclid* mission can constrain two templates of primordial undamped linear and logarithmic oscillations. In addition to the *Euclid*'s primary probes, i.e. the spectroscopic galaxy clustering and the combination of photometric surveys, we study the further constraints that will be added by *Euclid*'s measurements of the galaxy bispectrum and the information provided by future CMB experiments. The bispectrum is shown to be able to provide essential information on the parameters of the feature models, highlighting the importance of a high-order statistics analysis on the spectroscopic sample.

We structure the paper as follows. In Sect. 2, we introduce the physics of the adiabatic mode and we briefly review the diverse theoretical mechanisms that naturally generate features in the PPS, in particular realisations of inflation. In Sect. 3, we review *Euclid* specifications and calculation of the theoretical observables used in the Fisher forecast analysis. In Sect. 4 we start introducing the parametrised templates for primordial features with linear and logarithmic undamped oscillations. We then study the behaviour of these models on nonlinear scales of the matter power spectrum comparing the results from perturbation theory in Sect. 4.2 to N-body simulations in Sect. 4.3, and we study the numerical reconstruction of primordial features in Sect. 4.4. We present our results from primary *Euclid* observables in Sect. 5. We complement those by adding the information from the galaxy bispectrum in Sect. 6 and combining *Euclid* results with future CMB measurements in Sect. 7. We conclude in Sect. 8.

2. Primordial features and the early Universe

As mentioned in Sect. 1, the search for features in the primordial power spectrum has so far been statistically unsuccessful. On the largest scales, CMB observations agree with a red-tilted power-law PPS, $\mathcal{P}_{\mathcal{R},0}(k)$, with the following parametrisation

$$\mathcal{P}_{\mathcal{R},0}(k) = A_s \left(\frac{k}{k_*} \right)^{n_s-1}, \quad (1)$$

where A_s and n_s are the amplitude and the spectral index of the comoving curvature perturbations \mathcal{R} on superhorizon scales at the pivot scale $k_* = 0.05 \text{Mpc}^{-1}$.

The simplest class of models that can produce such a spectrum is known as canonical single-field slow-roll inflation. In these models a single scalar field — the inflaton — is responsible for both the primordial perturbations and the background evolution during inflation.¹

¹ These models are based additionally on other simplifying assumptions about the inflaton field, such as canonical kinetic terms, minimal

Unless the inflaton is the Higgs field (Bezrukov & Shaposhnikov 2008), inflation always takes us beyond the Standard Model (SM) of particle physics. While these scenarios can support cosmic inflation, it is rarely of the simplest kind. Beyond-SM models often involve multiple fields that interact with each other, and with the inflaton, and they can leave detectable imprints on the primordial perturbations including, for example, isocurvature modes and localised features. It is essential to have a bottom-up theoretical framework enabling us to analyse and classify all possible departures from the simplest scenario of Eq. (1) that are compatible with observations. Here we focus on the fluctuations as those are what we observe in the CMB and LSS. An important distinction is whether the curvature perturbations on superhorizon scales are generated by a single, possibly effective, degree of freedom. These are called effectively single field or ‘single clock’ models.

It can be shown that in the effective single-field slow-roll models the effective action for the comoving curvature perturbations is, to quadratic order,

$$S = \int d^4x a^3 M_{\text{Pl}}^2 \epsilon_1 \left[\frac{\dot{\mathcal{R}}^2}{c_s^2} - \frac{(\partial_i \mathcal{R})^2}{a^2} \right] + \dots, \quad (2)$$

where $a(t)$ is the scale factor, $c_s(t)$ is the speed of sound for curvature perturbations, and $\epsilon_1(t) \equiv -\dot{H}/H^2$ is the first slow-roll parameter; $H \equiv \dot{a}/a$ is the Hubble expansion rate, where the overdot denotes derivative with respect to the cosmic time t .

Eq. (2) is well known in the context of single-field slow-roll inflation, but it is much more general than that. It is the first term in a perturbative expansion — the effective field theory (EFT) of inflationary perturbations (Cheung et al. 2008) — where all the information about the background is systematically encoded in a set of functions (ϵ_1 and c_s being the first two) that describe what is seen by the perturbations.

This action describes almost all models of slow-roll inflation in which the primordial perturbations are generated by a single quantum field. It includes canonical single-field slow-roll models as a particular case ($c_s = 1$) but also any multi-field model in which the primordial perturbations are generated by a single quantum field (typically an effective low energy degree of freedom involving multiple high energy fields). The action in Eq. (2) is then obtained by integrating out the fast, or heavy, high energy degrees of freedom; see Achúcarro et al. (2012).

The idea behind the EFT approach is that what the perturbations see is an almost time-independent background, and this symmetry under time translations completely dictates the form of the action in Eq. (2), to all orders. The red tilt is a small deviation from perfect scale invariance, measured by the smallness of the slow-roll parameters. Any deviations from time-independence in the background functions result in features in the spectrum that can be calculated and cross-correlated among different observables; see Bartolo et al. (2013); Cannone et al. (2014) for applications of the EFT in the context of primordial oscillatory features.

In general, and depending on their origin, oscillatory features fall into two main classes which are the focus of this paper (see Achúcarro et al. 2022, for details and references). A small, abrupt change in the background functions $\epsilon_1(t)$ and $c_s(t)$ at a particular moment during inflation results in a transient oscillatory feature, linearly spaced in k , superimposed on the power spectrum (1). Two well studied examples are a step in the inflationary potential (Starobinsky 1992; Adams et al. 2001) and

coupling to gravity and the *Bunch-Davies* quantum vacuum for the perturbations.

a localised turn in the inflationary trajectory (Achúcarro et al. 2011; Chen 2012). The range of k where the oscillation persists increases with the sharpness of the change. But the sharpness cannot be arbitrarily large, since it should not excite the high energy modes that have been integrated out, nor enhance higher order terms that have been neglected in the perturbative expansion. On the other hand, oscillations logarithmically spaced in k are usually associated with periodicity in the background functions, for instance if there is a periodic modulation in the inflationary potential (Freese et al. 1990; Chen et al. 2008). More complicated combinations are also possible, that require a more tailored analysis. The upshot is that, if a feature is detected in the power spectrum, establishing its high energy origin will require stringent self-consistency checks, as well as correlated detections in other observables.

It is worth emphasising that the power of the EFT approach is that, since it is completely agnostic about the origin of the background expansion, it tests entire classes of models as opposed to individual ones. For example in multi-field models, ϵ_1 is related to the flatness of the potential along the inflationary trajectory, and c_s is related to the rate of turning of this trajectory in multi-field space. But the high energy origin of ϵ_1 and c_s may be completely different in other models.

3. *Euclid* probes

Euclid is one of the next generation deep- and large-field galaxy surveys. It will be able to measure up to 30 million spectroscopic redshifts, which can be used for galaxy clustering measurements, and 2 billion photometric galaxy images, which can be used for weak lensing observations.

Euclid will use near-IR (NIR) slitless spectroscopy to collect large samples of emission-line galaxies and to perform spectroscopic galaxy clustering measurements. The great advantage of this spectroscopic method is the high precision on measuring the redshift of the sources. However, one of the difficulties in inferring the cosmological parameters is given to the knowledge of the number density of the $H\alpha$ targets. The total number of galaxies that can be used in the analysis mostly depends on two factors: completeness and purity. Completeness is the fraction of objects correctly identified relative to the true number, whereas purity is defined as the fraction of objects correctly identified relative to the total number of detected objects. In practice, completeness represents the size of a sample, whereas purity is its quality. A lower value of the number density $n(z)$ of observed galaxies leads to an increase of the shot noise, resulting as a degradation on the constraints of the cosmological parameters.

One of the expected lensing observations is the cosmic shear, which is the distortion in the observed shapes of distant galaxies due to weak gravitational lensing by the LSS while the other probe comes from galaxy clustering using the positions of objects detected by the photometric measurements of redshifts. Given that both depend on the LSS density fluctuations as well as the geometry of the Universe, this will allow us to constrain the cosmological parameters. One of the main difficulties in using the weak lensing observable is the ability to accurately model the intrinsic alignments (IA) of galaxies that mimic the cosmological lensing signal. While for the galaxy clustering from photometric measurements, the main effects that need to be taken into account are the galaxy bias, accounting for the relation between the galaxy distribution and the underlying total matter distribution, and the photometric-redshift uncertainties, since redshift in this case is estimated from observing through multi-band filters instead of the full spectral energy distribution. Finally, an im-

portant issue for both the weak lensing and galaxy clustering probes is the modelling of the small-scale nonlinear clustering on the weak lensing two-point statistics that the high density of detected galaxies will allow us to reach.

In the following we detail on the prescription used in this work for our model for these two probes.

3.1. Spectroscopic galaxy clustering

Following [Euclid Collaboration: Blanchard et al. \(2020\)](#), we define the observed galaxy power spectrum as

$$P_{\text{obs}}(k_{\text{ref}}, \mu_{\text{ref}}; z) = \frac{1}{q_{\perp}^2 q_{\parallel}} \frac{1}{1 + k^2 \mu^2 f^2(z) \sigma_p^2(z)} \times \left[b(z) \sigma_8(z) + f(z) \sigma_8(z) \mu^2 \right]^2 \times \frac{P^{\text{IR, res, LO}}(k, \mu; z)}{\sigma_8^2(z)} F_z(k, \mu; z) + P_s(z), \quad (3)$$

where μ is the cosine of the angle of the wave mode with respect to the line of sight pointing into the direction \hat{r} . Here $b(z)$ is the linear clustering bias, $f(z)$ is the growth rate, and $\sigma_8(z)$ is the root mean square linearly evolved density fluctuations in spheres of $8 h^{-1} \text{Mpc}$.²

The Alcock-Paczynski (AP) effect ([Alcock & Paczynski 1979](#)), used to account for deviations of the cosmological models from the fiducial one, is parametrized through rescaling of the angular diameter distance $D_A(z)$ and the Hubble parameter $H(z)$, and enters as multiplicative factor through

$$q_{\perp}(z) = \frac{D_A(z)}{D_{A, \text{ref}}(z)} \quad \text{and} \quad q_{\parallel}(z) = \frac{H_{\text{ref}}(z)}{H(z)}, \quad (4)$$

where the subscript ref refers to the fiducial cosmology. This leads also to a rescaling of the wavevector components as

$$k_{\perp} = \frac{k_{\perp, \text{ref}}}{q_{\perp}} \quad \text{and} \quad k_{\parallel} = \frac{k_{\parallel, \text{ref}}}{q_{\parallel}}. \quad (5)$$

Using Eqs. (4) and (5) we can convert the known reference cosmology (k_{ref} and μ_{ref}) to the true unknown cosmology (k and μ),

$$k(k_{\text{ref}}, \mu_{\text{ref}}) = k_{\text{ref}} \alpha(\mu_{\text{ref}}), \quad (6)$$

$$\mu(\mu_{\text{ref}}) = \frac{\mu_{\text{ref}}}{\alpha(\mu_{\text{ref}}) q_{\parallel}}, \quad (7)$$

where

$$\alpha(\mu) = \left[\frac{\mu^2}{q_{\parallel}^2} + \frac{(1 - \mu^2)}{q_{\perp}^2} \right]^{1/2}. \quad (8)$$

The relations above can be used to define the effect of the choice of reference cosmology on the observed power spectrum via

$$P_{\text{obs}}(k_{\text{ref}}, \mu_{\text{ref}}; z) = \frac{1}{q_{\perp}^2 q_{\parallel}} P_g(k(k_{\text{ref}}), \mu(\mu_{\text{ref}}); z). \quad (9)$$

Galaxy bias, connecting the underlying dark matter (DM) power spectrum to the $H\alpha$ -line emitter galaxies detected by *Euclid*, is modelled by a simple linear clustering bias redshift-dependent coefficient $b(z)$. The anisotropic distortion to the density field due to the line-of-sight effects of the peculiar velocity

² h is the dimensionless Hubble parameter defined as $H_0 = 100 h \text{ km s}^{-1} \text{ Mpc}^{-1}$.

of the observed galaxy redshifts, known as redshift-space distortions (RSD), is modelled in the linear regime by the contribution in the square brackets introduced by [Kaiser \(1987\)](#). Linear RSD are corrected for the nonlinear finger-of-God (FoG) effect under the assumption of an exponential galaxy velocity distribution function as a Lorentzian ([Hamilton 1998](#)). The nonlinearities due to gravitational instabilities have the effect of smearing the baryon acoustic oscillations (BAO) signal, this is modelled through time-sliced perturbation theory (TSPT); we discuss the modelling of $P^{\text{IR, res, LO}}$ in Sect. 4.2. The pairwise velocity dispersion, $\sigma_p(z)$, is evaluated from the linear matter power spectrum as

$$\sigma_p^2(z) = \frac{1}{6\pi^2} \int_0^{k_{\text{max}}} dk P_{\text{lin}}(k, z). \quad (10)$$

The total galaxy power spectrum in Eq. (3) includes errors on the measurement of the redshift through the exponential factor

$$F_z(k, \mu; z) = e^{-k^2 \mu^2 \sigma_r^2(z)}, \quad (11)$$

where $\sigma_r^2(z) = c(1+z)\sigma_{0,z}/H(z)$ with $\sigma_{0,z}$ the error on the measured redshifts. Finally, we introduce a shot-noise term $P_s(z)$ due to imperfect removal of the Poisson sampling and the imperfect modelling of small scales.

The final Fisher matrix for the spectroscopic galaxy clustering (GC_{sp}) observable for one redshift bin z_i is

$$F_{\alpha\beta}(z_i) = \frac{1}{8\pi^2} \int_{-1}^1 d\mu \int_{k_{\text{min}}}^{k_{\text{max}}} k^2 dk V_{\text{eff}}(z_i, k) \times \frac{\partial \ln P_{\text{obs}}(k, \mu; z_i)}{\partial \theta_{\alpha}} \frac{\partial \ln P_{\text{obs}}(k, \mu; z_i)}{\partial \theta_{\beta}}, \quad (12)$$

where the derivatives are evaluated at the parameter values of the fiducial model and V_{eff} is the effective volume of the survey, given by

$$V_{\text{eff}}(k, \mu; z) = V_s \left[\frac{n(z) P_{\text{obs}}(k, \mu; z)}{1 + n(z) P_{\text{obs}}(k, \mu; z)} \right]^2, \quad (13)$$

where V_s is the volume of the survey and $n(z)$ is the number of galaxies in a redshift bin. Assuming that the observed power spectrum follows a Gaussian distribution, we write in Eq. (12) its covariance matrix as

$$\text{Cov}(k, k') \approx \frac{2(2\pi)^3}{V_{\text{eff}}(k, \mu; z)} P_{\text{obs}}^2(k, \mu; z) \delta^{\text{D}}(k - k'), \quad (14)$$

where $\delta^{\text{D}}(k - k')$ is the Dirac delta function.

We model the observed matter power spectrum of Eq. (3) in bandpowers averaged over a bandwidth of Δk with a top-hat window function as in [Huang et al. \(2012\)](#); [Ballardini et al. \(2016\)](#),

$$\hat{P}_{\text{obs}}(k, \mu; z) = \frac{1}{\Delta k} \int_{k-\Delta k/2}^{k+\Delta k/2} dk' P_{\text{obs}}(k', \mu; z). \quad (15)$$

The size of the k -bin Δk should be equal or larger than the effective fundamental frequency defined as $k_{\text{eff}} \equiv 2\pi/V^{1/3}$ for an ideal cubic volume in order to guarantee uncorrelated measurements of the observed power spectrum. The values of k_{eff} span in the range $0.0025\text{--}0.0031 h \text{ Mpc}^{-1}$ for a cubic volume for the four redshift bins. We assume a bin width of $\Delta k = 0.004 h \text{ Mpc}^{-1}$ with $k_{\text{min}} = 0.002 h \text{ Mpc}^{-1}$. Finally, we can rewrite the Fisher

matrix of Eq. 12 for the discrete number of averaged bandpower for the redshift bin z_i as

$$F_{\alpha\beta}(z_i) = \frac{1}{8\pi^2} \int_{-1}^1 d\mu \sum_{k=k_{\min}}^{k_{\max}} k^2 \Delta k V_{\text{eff}}(z_i, k) \times \frac{\partial \ln \hat{P}_{\text{obs}}(k, \mu; z_i)}{\partial \theta_\alpha} \frac{\partial \ln \hat{P}_{\text{obs}}(k, \mu; z_i)}{\partial \theta_\beta}. \quad (16)$$

The total spectroscopic Fisher matrix is then calculated by summing over the redshift bins as $F_{\alpha\beta}^{\text{SP}} = \sum_i F_{\alpha\beta}(z_i)$, assuming that the redshift bins are independent. Since we are interested in the standard cosmological parameters and the feature parameters, we marginalise the GC_{sp} Fisher matrix over two redshift-dependent parameters $b\sigma_8(z_i)$ and $P_s(z_i)$ for each of the four redshift bins.

3.2. Photometric galaxy clustering and weak lensing

Both the forecasting method and the tools used for the photometric analyses are the same as the ones in [Euclid Collaboration: Blanchard et al. \(2020\)](#) apart from the changes in the power spectrum due to the primordial features in the predicted *Euclid* observables. Here we only remind the reader of the main steps.

The observables we consider are the angular power spectra $C_{ij,\ell}^{XY}$ between probe X in the i -th redshift bin and probe Y in the j -th redshift bin, where the probes X and Y are L for weak lensing or G for photometric galaxy clustering; $C_{ij,\ell}^{XY}$ therefore refers to both auto- and cross-correlations of these probes. Relying on the Limber approximation and within the flat sky limit, the spectra are given by

$$C_{ij,\ell}^{XY} = c \int_{z_{\min}}^{z_{\max}} dz \frac{W_i^X(z) W_j^Y(z)}{H(z) r^2(z)} P_{\text{NL}}(k_\ell, z), \quad (17)$$

with $k_\ell = (\ell + 1/2)/r(z)$, $r(z)$ the comoving distance to redshift z , and $P_{\text{NL}}(k_\ell, z)$ the nonlinear power spectrum of matter density fluctuations at wave number k_ℓ and redshift z . The GC_{ph} and WL window functions read

$$W_i^G(z) = b_i(z) n_i(z) \frac{H(z)}{c}, \quad (18)$$

$$W_i^L(z) = \frac{3}{2} \Omega_{\text{m},0} \left(\frac{H_0}{c} \right)^2 (1+z) r(z) \int_z^{z_{\max}} dz' n_i(z') \left[1 - \frac{r(z)}{r(z')} \right] + W_i^{\text{IA}}(z), \quad (19)$$

where $b_i(z)$ is the galaxy bias in the i -th redshift bin, and $W_i^{\text{IA}}(z)$ encodes the contribution of IA to the WL power spectrum. The normalised number density distribution $n_i(z)$ of observed galaxies in the i -th redshift bin is given by

$$n_i(z) = \frac{\int_{z_i^-}^{z_i^+} dz' n(z) p_{\text{ph}}(z'|z)}{\int_{z_{\min}}^{z_{\max}} dz \int_{z_i^-}^{z_i^+} dz' n(z) p_{\text{ph}}(z'|z)}, \quad (20)$$

where (z_i^-, z_i^+) are the edges of the i -th redshift bin and $n(z)$ is the underlying true redshift distribution. The true number density of galaxies is convolved with the probability distribution function $p_{\text{ph}}(z'|z)$ is given following the parameterization in [Euclid Collaboration: Blanchard et al. \(2020\)](#).

The IA contribution is computed following the extended nonlinear alignment (eNLA) model adopted in [Euclid Collaboration: Blanchard et al. \(2020\)](#) so that the corresponding window function is

$$W_i^{\text{IA}}(z) = -\frac{\mathcal{A}_{\text{IA}} C_{\text{IA}} \Omega_{\text{m},0} \mathcal{F}_{\text{IA}}(z)}{D(z)} n_i(z) \frac{H(z)}{c}, \quad (21)$$

where

$$\mathcal{F}_{\text{IA}}(z) = (1+z)^{\eta_{\text{IA}}} \left[\frac{\langle L \rangle(z)}{L_\star(z)} \right]^{\beta_{\text{IA}}}, \quad (22)$$

with $\langle L \rangle(z)$ the redshift-dependent mean, and $L_\star(z)$ the characteristic luminosity of source galaxies as computed from the luminosity function. \mathcal{A}_{IA} , β_{IA} and η_{IA} are the nuisance parameters of the model, and C_{IA} is a constant accounting for dimensional units.

We consider a Gaussian-only covariance whose elements are given by

$$\text{Cov} \left[C_{ij,\ell}^{\text{AB}}, C_{mn,\ell'}^{\text{CD}} \right] = \frac{\delta_{\ell\ell'}^{\text{K}}}{(2\ell+1) f_{\text{sky}} \Delta\ell} \times \left\{ \left[C_{im,\ell}^{\text{AC}} + \mathcal{N}_{im,\ell}^{\text{AC}} \right] \left[C_{jn,\ell'}^{\text{BD}} + \mathcal{N}_{jn,\ell'}^{\text{BD}} \right] + \left[C_{in,\ell}^{\text{AD}} + \mathcal{N}_{in,\ell}^{\text{AD}} \right] \left[C_{jm,\ell'}^{\text{BC}} + \mathcal{N}_{jm,\ell'}^{\text{BC}} \right] \right\}, \quad (23)$$

where the upper- and lower-case Latin indices run over L and G (all tomographic bins), $\delta_{\ell\ell'}^{\text{K}}$ is the Kronecker delta coming from the lack of correlation between different multipoles (ℓ, ℓ'), f_{sky} is the survey's sky fraction, and $\Delta\ell$ denotes the width of the logarithmic equi-spaced multipole bins. We consider a white noise,

$$\mathcal{N}_{ij,\ell}^{\text{LL}} = \frac{\delta_{ij}^{\text{K}}}{\bar{n}_i} \sigma_\epsilon^2, \quad \mathcal{N}_{ij,\ell}^{\text{GG}} = \frac{\delta_{ij}^{\text{K}}}{\bar{n}_i}, \quad \mathcal{N}_{ij,\ell}^{\text{GL}} = 0, \quad (24)$$

where σ_ϵ is the variance of observed ellipticities.

For evaluating the Fisher matrix $F_{\alpha\beta}^{\text{ph}}$ for the observed galaxy power spectrum, we use

$$F_{\alpha\beta}^{\text{ph}} = \sum_{\ell=\ell_{\min}}^{\ell_{\max}} \sum_{ij,mm} \frac{\partial C_{ij,\ell}^{\text{AB}}}{\partial \theta_\alpha} \text{Cov}^{-1} \left[C_{ij,\ell}^{\text{AB}}, C_{mn,\ell}^{\text{CD}} \right] \frac{\partial C_{mn,\ell}^{\text{CD}}}{\partial \theta_\beta}. \quad (25)$$

3.3. Survey specifications

Following [Euclid Collaboration: Blanchard et al. \(2020\)](#), we consider for the spectroscopic sample four redshift bins centred at $\{1.0, 1.2, 1.4, 1.65\}$, whose widths are $\Delta z = 0.2$ for the first three bins and $\Delta z = 0.3$ for the last bin. The $H\alpha$ bias, evaluated at the central redshift of the bins, corresponds to $\{1.46, 1.61, 1.75, 1.90\}$. The number density of galaxies $n(z)$ corresponds to $\{6.86, 5.58, 4.21, 2.61\} \times 10^{-4}$.

For the photometric probes, the sources are split into 10 equi-populated redshift bins whose limits are obtained from the redshift distribution

$$n(z) \propto \left(\frac{z}{z_0} \right)^2 \exp \left[- \left(\frac{z}{z_0} \right)^{3/2} \right], \quad (26)$$

with $z_0 = 0.9/\sqrt{2}$ and the normalisation set by the requirement that the surface density of galaxies is $\bar{n}_g = 30 \text{ arcmin}^{-2}$. This is then convolved with the sum of two Gaussians to account for the effect of photometric redshift (see [Euclid Collaboration: Blanchard et al. 2020](#), for details). The galaxy bias is assumed to be constant within each redshift bin, with fiducial values $b_i = \sqrt{1 + \bar{z}_i}$, where \bar{z}_i is the bin centre. We consider 100 logarithmic equi-spaced multipole bins with $\sigma_\epsilon = 0.3$ the variance of observed ellipticities. We set $(z_{\min}, z_{\max}) = (0.001, 4)$, which spans the full range where the source redshift distributions $n_i(z)$ are non-vanishing.

For all the *Euclid* probes the survey's sky fraction is $f_{\text{sky}} \approx 0.36$ ([Euclid Collaboration: Scaramella et al. 2022](#)).

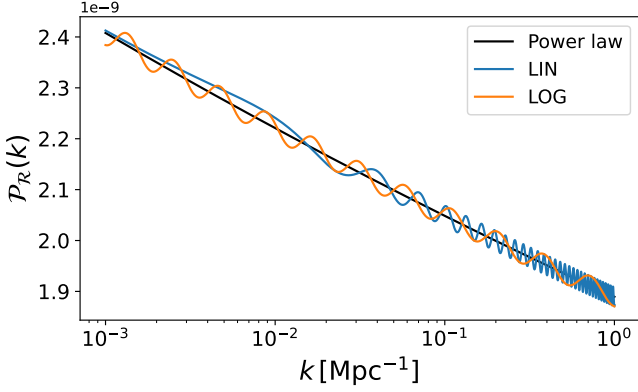


Fig. 1. Primordial power spectrum of curvature perturbations for linear (LIN) and logarithmic (LOG) feature models with fiducial parameter values given in (29) and (30).

4. Theoretical modelling of primordial features in galaxy surveys

As representative models for features in primordial fluctuations in this paper we consider oscillations linearly and logarithmically spaced in Fourier space with a constant amplitude superimposed to a power spectrum described by a power-law.

4.1. Models

We consider a superimposed pattern of oscillations as

$$\mathcal{P}_{\mathcal{R}}(k) = \mathcal{P}_{\mathcal{R},0}(k) \left[1 + \delta P^X(k) \right], \quad (27)$$

where $\mathcal{P}_{\mathcal{R},0}(k)$ is the standard power-law PPS of the comoving curvature perturbations \mathcal{R} on superhorizon scales, given in Eq. (1). We study the following templates with superimposed oscillations on the PPS

$$\delta P^X(k) = \mathcal{A}_X \sin(\omega_X \Xi_X + 2\pi\phi_X), \quad (28)$$

where $X = \{\text{lin}, \text{log}\}$ and $\Xi_X = \{k/k_*, \ln(k/k_*)\}$.

We choose the fiducial cosmological parameters according to *Planck* DR3 mean values of the marginalised posterior distributions (Planck Collaboration: Aghanim et al. 2020b): $\omega_b = 0.02237$, $\omega_c = 0.1200$, $H_0 = 67.36 \text{ km s}^{-1} \text{ Mpc}^{-1}$, $\ln(10^{10} A_s) = 3.044$, $n_s = 0.9649$, $\sigma_8 = 0.8107$, and $m_\nu = 0.06 \text{ eV}$ (with one massive neutrino and two massless ones). In what follows we specify the fiducial values of the model parameters.

1. Linear oscillations:

$$\Theta_{\text{lin}} = \left\{ \mathcal{A}_{\text{lin}} = 0.01, \omega_{\text{lin}} = 10, \phi_{\text{lin}} = 0 \right\}. \quad (29)$$

2. Logarithmic oscillations:

$$\Theta_{\text{log}} = \left\{ \mathcal{A}_{\text{log}} = 0.01, \omega_{\text{log}} = 10, \phi_{\text{log}} = 0 \right\}. \quad (30)$$

We show the effect of the feature parameters on the PPS in Fig. 1.

4.2. Modelling nonlinear scales in perturbation theory in the presence of primordial oscillatory features

The linearly propagated matter power spectrum is given by

$$P_{\text{lin}}(k, z) = M^2(k, z) P_{\Phi}(k), \quad (31)$$

where $M(k, z) = 2k^2 c^2 T(k) D(z) / (3\Omega_m H_0^2)$, with $T(k)$ the matter transfer function normalised to unity at large scales (i.e. $k \rightarrow 0$) and c the speed of light. The gravitational potential power spectrum will then be derived from the two oscillatory models considered: $P_{\Phi} = 9/25(2\pi^2) \mathcal{P}_{\mathcal{R}}(k)/k^3$.

Our analytic model for the matter power spectrum is based on TSPT and it takes into account the damping of oscillations by infrared (IR) resummation of the large-scale bulk flows (Crocco & Scoccimarro 2008; Creminelli et al. 2014; Baldauf et al. 2015; Blas et al. 2016b; Senatore & Trevisan 2018). The implementation of the IR resummation can be done following the approach to BAO in the context of TSPT (Blas et al. 2016a,b). We start by decomposing the linear matter power spectrum into a smooth (or no-wiggle; nw) and an oscillating (w) contribution,

$$P_{\text{lin}}(k, z) = D^2(z) [P_{\text{nw}}(k) + P_w(k)], \quad (32)$$

where P_{nw} is the no-wiggle power spectrum, and the oscillatory part P_w describes both the BAO feature and the primordial oscillating feature as

$$P_w(k) \equiv P_{\text{nw}} \left[\delta P_w^{\text{BAO}}(k) + \delta P_w^X(k) + \delta P_w^{\text{BAO}}(k) \delta P_w^X(k) \right]. \quad (33)$$

Here we have factored out the time-dependence given by the growth factor $D(z)$. We have neglected the cross term in Eq. (33) as it is proportional to $A_{\text{BAO}} \times \mathcal{A}_{\text{lin}}$ and therefore subdominant. We filter the BAO feature from the linear matter power spectrum using a Savitzky-Golay filter; see Boyle & Komatsu (2018).

At next-to-leading order (NLO), the IR resummed power spectrum for linear oscillations can be written as (Blas et al. 2016b; Beutler et al. 2019)

$$\begin{aligned} P_{\text{IR res, LO+NLO}}(k, z) &= D^2(z) P_{\text{nw}}(k) \\ &\times \left\{ 1 + \left[1 + k^2 D^2(z) \Sigma_{\text{BAO}}^2 \right] e^{-k^2 D^2(z) \Sigma_{\text{BAO}}^2} \delta P_w^{\text{BAO}}(k) \right. \\ &+ \left. \left[1 + k^2 D^2(z) \Sigma_{\text{lin}}^2 \right] e^{-k^2 D^2(z) \Sigma_{\text{lin}}^2} \delta P_w^{\text{lin}}(k) \right\} \\ &+ D^4(z) P^{1\text{-loop}} \left[P_{\text{IR res, LO}}(k) \right], \end{aligned} \quad (34)$$

and for logarithmic oscillations as (Vasudevan et al. 2019; Beutler et al. 2019)

$$\begin{aligned} P_{\text{IR res, LO+NLO}}(k, z) &= D^2(z) P_{\text{nw}}(k) \\ &\times \left\{ 1 + \left[1 + k^2 D^2(z) \Sigma_{\text{BAO}}^2 \right] e^{-k^2 D^2(z) \Sigma_{\text{BAO}}^2} \delta P_w^{\text{BAO}}(k) \right. \\ &+ \left. \left[1 + k^2 D^2(z) \Sigma_{\text{log}}^2 \right] e^{-k^2 D^2(z) \Sigma_{\text{log}}^2} \left[\cos(k^2 D^2(z) \hat{\Sigma}_{\text{log}}^2) \delta P_w^{\text{log}}(k) \right. \right. \\ &\left. \left. - \sin(k^2 D^2(z) \hat{\Sigma}_{\text{log}}^2) \frac{d \delta P_w^{\text{log}}(k)}{\omega_{\text{log}} d \ln k} \right] \right\} \\ &+ D^4(z) P^{1\text{-loop}} \left[P_{\text{IR res, LO}}(k) \right]. \end{aligned} \quad (35)$$

$P^{1\text{-loop}}$ is the standard one-loop result, but computed with the leading-order (LO) IR resummed power spectrum. We take the usual expression $P^{1\text{-loop}} = P_{22} + 2P_{13}$ with

$$P_{22}(k) = \int \frac{d^3 q}{4\pi^3} F_2^2(\mathbf{q}, \mathbf{k} - \mathbf{q}) P_{\text{lin}}(q) P_{\text{lin}}(|\mathbf{k} - \mathbf{q}|), \quad (36)$$

$$P_{13}(k) = 3P_{\text{lin}}(k) \int \frac{d^3 q}{4\pi^3} F_3(\mathbf{q}, -\mathbf{q}, \mathbf{k}) P_{\text{lin}}(q), \quad (37)$$

while evaluating the loop integrals P_{22} and P_{13} with the input spectrum $P^{\text{IR res, LO}}$ instead of the linear spectrum (Blas et al. 2016a). F_n are the usual perturbation theory (PT) kernels (Bernardeau et al. 2002). We calculate these quantities, i.e. Eqs. (36) and (37), with the publicly available code FAST-PT (McEwen et al. 2016; Fang et al. 2017).³ The IR resummed power spectrum at leading order is given by

$$P^{\text{IR res, LO}}(k, z) = D^2(z)P_{\text{nw}}(k) \times \left[1 + e^{-k^2 D^2(z)\Sigma_{\text{BAO}}^2} \delta P_{\text{w}}^{\text{BAO}}(k) + e^{-k^2 D^2(z)\Sigma_{\text{lin}}^2} \delta P_{\text{w}}^{\text{lin}}(k) \right] \quad (38)$$

for the linear oscillations (Blas et al. 2016b; Beutler et al. 2019) and by

$$P^{\text{IR res, LO}}(k, z) = D^2(z)P_{\text{nw}}(k) \times \left[1 + e^{-k^2 D^2(z)\Sigma_{\text{BAO}}^2} \delta P_{\text{w}}^{\text{BAO}}(k) + e^{-k^2 D^2(z)\Sigma_{\text{log}}^2} \cos\left(k^2 D^2(z)\hat{\Sigma}_{\text{log}}^2\right) \delta P_{\text{w}}^{\text{log}}(k) - e^{-k^2 D^2(z)\Sigma_{\text{log}}^2} \sin\left(k^2 D^2(z)\hat{\Sigma}_{\text{log}}^2\right) \frac{d\delta P_{\text{w}}^{\text{log}}(k)}{\omega_{\text{log}} d \ln k} \right] \quad (39)$$

for the logarithmic oscillations (Vasudevan et al. 2019; Beutler et al. 2019). The result of the IR resummation at LO is given by a first contribution corresponding to the smooth part of the linear power spectrum and a second contribution corrected by the exponential damping of the oscillatory part due to the effect of IR enhanced loop contributions. The result for the logarithmic oscillations has additional contributions, on top of scale-dependent damping factors, due to the non-trivial oscillatory behaviour in real space. The damping factors above correspond to

$$\Sigma_{\text{BAO}}^2(k_S) \equiv \int_0^{k_S} \frac{dq}{6\pi^2} P_{\text{nw}}(q) [1 - j_0(qr_s) + 2j_2(qr_s)], \quad (40)$$

$$\Sigma_{\text{lin}}^2(\omega_{\text{lin}}, k_S) \equiv \int_0^{k_S} \frac{dq}{6\pi^2} P_{\text{nw}}(q) \left[1 - j_0\left(q \frac{\omega_{\text{lin}}}{k_*}\right) + 2j_2\left(q \frac{\omega_{\text{lin}}}{k_*}\right) \right], \quad (41)$$

$$\Sigma_{\text{log}}^2(k, \omega_{\text{log}}, k_S) \equiv \int_0^{k_S} \frac{dq}{4\pi^2} P_{\text{nw}}(q) \times \int_{-1}^1 d\mu \mu^2 \left\{ 1 - \cos\left[\omega_{\text{log}} \ln\left(1 - \frac{q\mu}{k}\right)\right] \right\}, \quad (42)$$

$$\hat{\Sigma}_{\text{log}}^2(k, \omega_{\text{log}}, k_S) \equiv - \int_0^{k_S} \frac{dq}{4\pi^2} P_{\text{nw}}(q) \int_{-1}^1 d\mu \mu^2 \sin\left[\omega_{\text{log}} \ln\left(1 - \frac{q\mu}{k}\right)\right], \quad (43)$$

where j_n are spherical Bessel functions, $r_s \simeq 147$ Mpc is the scale setting the period of the BAO (Planck Collaboration: Aghanim et al. 2020b), and k_S is the separation scale controlling the modes which are to be resummed. The dependence on k_S can be connected with an estimate of the theoretical perturbative uncertainties. For this reason and since IR expansions are valid for $q \ll k$, we assume $k_S = \epsilon k$ with $\epsilon \in [0.3, 0.7]$ (Baldauf et al. 2015; Vasudevan et al. 2019).

In redshift space, the damping factor becomes also dependent on the cosine μ since peculiar velocities additionally wash out wiggle signals along the line of sight. In this case, we have at leading order (Eisenstein et al. 2007) in Eqs. (38) and (39) $D(z)\Sigma_X \rightarrow D(z)\Sigma_X(\mu)$ with

$$\Sigma_X^2(k, \mu, z) = \Sigma_X^2(z) \left\{ 1 - \mu^2 + \mu^2 [1 + f(k, z)]^2 \right\}. \quad (44)$$

³ <https://github.com/JoeMcEwen/FAST-PT>

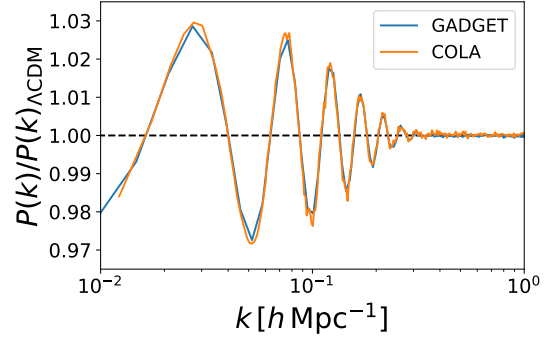


Fig. 2. Ratio with respect to the Λ CDM case of the nonlinear matter power spectra in Fourier space at redshift $z = 0$ calculated with the approximate N-body method COLA and with the full N-body code GADGET-3 for the linear oscillations with $\mathcal{A}_{\text{lin}} = 0.03$ and $\omega_{\text{lin}} = 10$ (Ballardini et al. 2020).

We note that while in the next subsection, Sect. 4.3, we present both PT results at LO and NLO, that is Eqs. (38)-(39)-(34)-(35), and we compare them to N-body simulations. Furthermore, we only used the LO to derive the Fisher-matrix uncertainties in Sect. 5.

For the nonlinear modelling for photometric probes, entering Eq. (17), we use a modified version of HMCODE (Mead et al. 2016) where the Λ CDM nonlinear matter power spectrum is dressed with the primordial oscillations according to

$$P_{\text{NL}}(k, z) = \frac{P_{\text{NL}}^{\Lambda\text{CDM}}(k, z)}{P_{\text{lin}}^{\Lambda\text{CDM}}(k, z)} P^{\text{IR res, LO}}(k, z). \quad (45)$$

4.3. Comparing predictions of perturbation theory with N-body simulations

We produce cosmological simulations based on the Comoving Lagrangian Approximation (COLA) method (Tassev et al. 2013, 2015; Winther et al. 2017; Wright et al. 2017) in order to assess the accuracy of the predictions of PT at LO and NLO for the template (28) using a modified version of the publicly available code L-PICOLA (Howlett et al. 2015).⁴ We fix the standard cosmological parameters and the amplitude and phase of the feature, and we study the effect of varying the frequency of the primordial oscillations over the set of values $\omega_X \in \{0.2, 0.4, 0.6, 0.8, 1, 1.2, 1.4, 1.6, 1.8, 2\}$. Following the analysis done by Ballardini & Finelli (2022), we run each simulation with 1024^3 dark matter particles in a comoving box with side length of $1024 h^{-1}$ Mpc evolved with 30 time steps. We set at redshift $z = 9$ the initial conditions that we generate using second-order Lagrangian perturbation theory, with the 2LPTic code (Crocce et al. 2006). Finally, we use spectra averaged over pairs of simulations with the same initial seeds and inverted initial conditions, and with amplitude fixing in order to minimise the cosmic variance (Viel et al. 2010; Villaescusa-Navarro et al. 2018). In Fig. 2, we show a comparison between the nonlinear matter power spectrum at $z = 0$ simulated with COLA and the one obtained by Ballardini et al. (2020) at the same resolution with the N-body code GADGET-3, a modified version of the publicly available code GADGET-2 (Springel et al. 2001; Springel 2005),⁵ for $\mathcal{A}_{\text{lin}} = 0.03$ and $\omega_{\text{lin}} = 10$.

⁴ <https://github.com/CullanHowlett/l-picola>

⁵ <https://wwwmpa.mpa-garching.mpg.de/gadget>

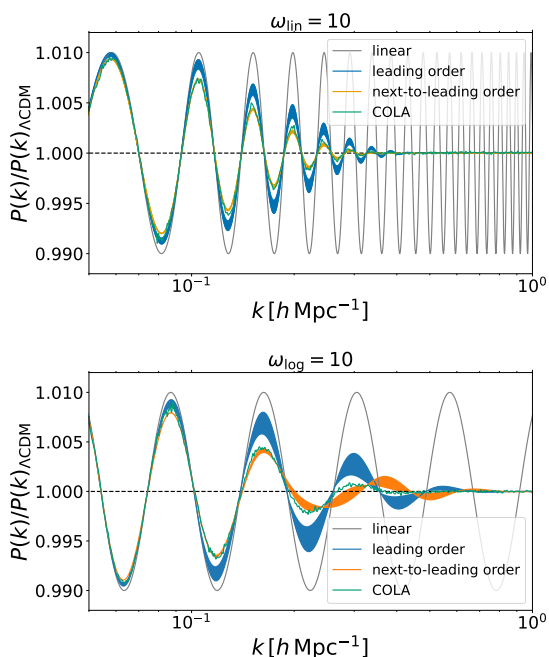


Fig. 3. Ratio of IR resummed matter power spectrum at LO (blue) and NLO (orange) obtained for linear (top panel) and logarithmic (bottom panel) oscillations to the one obtained with a power-law PPS at redshift $z = 0$ when the frequency $\omega_x = 10$ and the IR separation scale $k_s = \epsilon k$ is varied (with $\epsilon \in [0.3, 0.7]$). We also show the results of the linear theory (grey) and the ones obtained from N-body simulations (green).

We show in Fig. 3 the ratio between the matter power spectrum with primordial oscillations and the one with featureless PPS calculated at redshift $z = 0$ for the results both at LO and NLO for the two templates with linear and logarithmic oscillations. We collect in Appendix A the results for different frequencies; see Figs. A.1 and A.2.

For the template with undamped linear oscillations, the agreement between N-body simulations and PT results is remarkable for the entire range of frequencies considered, i.e. $\log_{10} \omega_{\text{lin}} \in (0.2, 2)$. At LO, we find differences for the matter power spectrum in Fourier space at redshift $z = 0$ less than 1% for $\log_{10} \omega_{\text{lin}} > 0.6$ and between 1% and 2% for $\log_{10} \omega_{\text{lin}} \leq 0.6$. At NLO, we find an agreement better than 1% for all the frequencies and differences $< 0.5\%$ for $\log_{10} \omega_{\text{lin}} > 0.4$. For the template with undamped logarithmic oscillations, we find a similar agreement for the frequencies $\log_{10} \omega_{\text{log}} \geq 1$, less than 1% for the LO and less than 0.5% for the NLO. In order to improve the accuracy of the results for low frequencies (see Beutler et al. 2019, for a discussion on the validity of perturbation approach for small frequencies) we can fit a Gaussian damping to the N-body simulation as done by Ballardini et al. (2020).

While we restrict the validation of results to the matter power spectrum in real space, a validation for the halo power spectrum in redshift space has been performed by Chen et al. (2020), showing that current results from PT are able to describe redshift-space clustering observables also in the presence of primordial features.

4.4. Nonlinear reconstruction of primordial features

An alternative to the modelling approach described above is through reconstruction. This takes the opposite logic, by starting from an evolved, nonlinear, matter field where the primor-

dial oscillations have been damped, it tries to recover their undamped states. Reconstruction has long been adopted as a useful technique to undo the effect of structure evolution and retrieve sharper BAO features, hence improving their use as a standard ruler to constrain cosmological parameters (Eisenstein et al. 2007; Wang et al. 2017; Sarpa et al. 2019), with an even longer history of applications in other subfields of cosmology and astrophysics (Peebles 1989; Croft & Gaztanaga 1997; Monaco & Efstathiou 1999; Nusser & Branchini 2000; Brenier et al. 2003; Mohayaee et al. 2003; Schmittfull et al. 2017; Zhu et al. 2017; Shi et al. 2018; Birkin et al. 2019; Mao et al. 2021).

From the point of view of reconstruction, there is no fundamental difference between BAO features and features that exist in the primordial density fluctuations on similar length scales: both are present at the time of last scattering, the preservation of both is negatively impacted by late-time cosmic structure formation, and both can be at least partially recovered if such an impact is undone through processes such as reconstruction (Beutler et al. 2019; Li et al. 2022). Therefore, we expect that reconstruction can find uses in the study of primordial features, at least when the oscillations have similar frequencies as the BAO peaks, $0.05 \lesssim k/(h \text{ Mpc}^{-1}) \lesssim 0.5$ — at scales much larger than this range any significant damping of the features due to cosmological evolution is yet to happen, because structure formation is hierarchical and affects smaller scales first, while on much smaller scales reconstruction becomes unreliable.

Another useful property of reconstruction is that it is possible to include galaxy bias (Birkin et al. 2019) and RSD (Monaco & Efstathiou 1999; Burden et al. 2014; Hada & Eisenstein 2018, 2019; Wang et al. 2020) in the pipeline, so that two of the most important theoretical systematic effects in analysing the galaxy redshift power spectrum are taken into account. Of course, caution is due here to ensure that the range of length scales where reconstruction from a catalogue of redshift-space biased tracers can be done reliably covers the range where we hope reconstruction to also benefit the recovery of the primordial features of interest. Checking this naturally requires a more detailed analysis, which may also depend on the reconstruction algorithm in actual use: while a quantitative analysis of this issue is not the topic here, our experience is that the scale range $k \lesssim 0.2 h \text{ Mpc}^{-1}$ or $s \gtrsim 15\text{--}20 h^{-1} \text{ Mpc}$ satisfies these requirements.

In this work, we exemplify using the nonlinear reconstruction method described in Shi et al. (2018); Birkin et al. (2019); Wang et al. (2020). Other algorithms may give quantitatively different results, though we do not expect a huge variation among the ones that are at an advanced stage of development. The problem of reconstruction can be reduced to identifying a mapping between the initial, Lagrangian coordinate of some particle, \mathbf{q} , and its Eulerian coordinate after evolution, $\mathbf{x}(t)$, at a later time t . If trajectory crossings of particles have not happened, this mapping is unique and can be obtained by solving the mass conservation equation

$$\rho(\mathbf{x}) d^3 \mathbf{x} = \rho(\mathbf{q}) d^3 \mathbf{q} \approx \bar{\rho} d^3 \mathbf{q}, \quad (46)$$

where $\rho(\mathbf{q})$ and $\rho(\mathbf{x})$ are, respectively, the initial density field in some infinitesimal volume element $d\mathbf{q}$, and the density field in the same volume element at time t , which now has been moved, and possibly deformed, and described by $d\mathbf{x}$. As the density field in the early Universe is homogeneous to a very good approximation, one can take $\rho(\mathbf{q})$ to be a constant, i.e. $\rho(\mathbf{q}) \approx \bar{\rho}$.

We define the displacement field Ψ between the final and initial positions of a particle as $\Psi(\mathbf{x}) = \mathbf{x} - \mathbf{q}$, which can be rewritten as

$$\nabla_{\mathbf{x}} \Theta(\mathbf{x}) \equiv \mathbf{q} = \mathbf{x} - \Psi(\mathbf{x}), \quad (47)$$

with $\Theta(\mathbf{x})$ being the displacement potential. Here we have assumed the displacement field to be curl-free, i.e. $\nabla \times \Psi = \mathbf{0}$, which is valid only on large scales.⁶ Combining Eq. (47) and Eq. (46) gives

$$\det[\nabla^i \nabla_j \Theta(\mathbf{x})] = \frac{\rho(\mathbf{x})}{\bar{\rho}} \equiv 1 + \delta(\mathbf{x}), \quad (48)$$

where $\delta(\mathbf{x}) = \rho(\mathbf{x})/\bar{\rho} - 1$ is the density contrast at time t , ‘det’ is the determinant of a matrix, here the Hessian of $\Theta(\mathbf{x})$, and $i, j = 1, 2, 3$. Shi et al. (2018) proposed to solve this equation as a nonlinear partial differential equation with cubic power of second-order derivatives of Θ . This was later extended by Birkin et al. (2019) to cases where $\delta(\mathbf{x})$ in the above can be the density contrast of some biased tracers of the dark matter field, such as galaxies and dark matter haloes.

Once $\Theta(\mathbf{x})$ is solved, one can obtain $\Psi(\mathbf{x})$ and the reconstructed density field is given by

$$\delta_r = -\nabla_q \cdot \Psi(\mathbf{q}), \quad (49)$$

where we express Ψ in terms of the Lagrangian coordinate \mathbf{q} , since the divergence ∇_q therein is with respect to \mathbf{q} . This calculation means that we need to have $\Psi(\mathbf{q})$ on a regular \mathbf{q} -grid, which can be done using, for example the Delaunay Tessellation Field Estimator code (DTFE; Schaap & van de Weygaert 2000; van de Weygaert & Schaap 2009; Cautun & van de Weygaert 2011), by interpolating $\Psi(\mathbf{x})$ to the target \mathbf{q} -grid.

The quantity δ_r obtained above is an approximation to the initial linear matter density contrast, linearly extrapolated to time t (bearing in mind that all the discussion in this subsection is for Λ CDM, for which the linear growth factor is scale-independent). As a result, part of the structure-formation-induced damping of the BAO or primordial features imprinted in the density field can be undone this way.

The damping of the BAO or primordial wiggles can be described by a Gaussian fitting function (cf. Sect. 4.3; Vasudevan et al. 2019; Beutler et al. 2019; Ballardini et al. 2020), effectively multiplying the undamped power spectrum wiggles O_w^{undamped} by a Gaussian function

$$O_w^{\text{damped}}(k, z) = O_w^{\text{undamped}}(k, z) \exp\left[-\frac{k^2 \zeta(z)^2}{2}\right], \quad (50)$$

where $\zeta(z)$ is the parameter quantifying the level of damping. In the linearly evolved density field with no damping, one has $\zeta = 0$. For the evolved nonlinear matter or galaxy field, $\zeta > 0$ with its values depending on redshift, tracer type, tracer number density etc., and the reconstructed density field generally features a smaller yet positive value of ζ .

We generate a suite of N-body simulations using the initial conditions described in Sect. 4.3, which includes a no-wiggle model and 20 wiggled models. The simulations are performed using the parallel N-body code *ramses* (Teyssier 2002). We output 4 snapshots of the DM respectively at $z = 1.5, 1.0, 0.5$ and 0, and measure the matter power spectrum of each of the snapshots. We follow the same reconstruction pipeline employed in Li et al. (2022) to reconstruct the density fields from each of the snapshots for all the models (shown in Fig. B.1). We have

⁶ This is similar to the assumption of no particle trajectory crossing, which must break down on small scales. Together, these assumptions mean that the reconstruction method described here, similar to other reconstruction methods, should only be expected to work for relatively large scales, and its performance progressively degrades if one goes to smaller scales.

Table 1. Best-fit values of $\zeta(z)$ for unreconstructed (reconstructed) wiggle spectra.

z	unrec	rec	efficiency
0.0	8.16	2.04	4.00
0.5	6.49	1.69	3.84
1.0	5.23	1.41	3.71
1.5	4.32	1.21	3.57

Notes. Columns respectively denote (1) redshift, (2) unreconstructed wiggles, (3) reconstructed wiggles, and (4) reconstruction efficiency (defined as $\zeta_{\text{unrec}}/\zeta_{\text{rec}}$).

also performed reconstruction from halo catalogues, though the results are noisier and not shown here; the DM reconstruction result can be considered as an ideal scenario, which serves as a limit of what can be achieved from halo or galaxy reconstruction with increasing tracer number density. We present the reconstruction from mock galaxy catalogues in redshift space based on the same set of simulations in a separate work. Fig. B.1 shows that reconstruction can help recover the weakened wiggles down to $k \approx 1 h \text{Mpc}^{-1}$. Note that, in order to avoid artificial features in the $P(k)$ of the models with high-frequency wiggles, we have binned $P(k)$ in k bins of width $0.001 h \text{Mpc}^{-1}$.

To estimate the best-fit values of $\zeta(z)$, the Gaussian function is applied to fit the envelopes of the unreconstructed and reconstructed wiggled spectra, $O_w^{\text{damped}}(k, z)$. We apply the Hilbert transform to measure the wiggle envelopes for each wiggled model and each redshift. Nevertheless, we expect that the damping parameter $\zeta(z)$, for both the unreconstructed and the reconstructed cases, should mostly depend on the nonlinear structure formation and be insensitive to the wiggle model, given that the wiggles are weak. We have explicitly checked this by comparing the envelopes of O_w^{damped} and O_w^{undamped} of the different models, and finding them to agree very well. As a result, to get $\zeta(z)$, the O_w envelopes of all wiggle models at redshift z could be combined to do a single least-squares fitting. In practice, because the measurement of the envelopes is not very reliable for the low-frequency featured models due to the very few wiggles in the k range of fitting, $k = (0.05-1) h \text{Mpc}^{-1}$, we select only the 10 high-frequency feature models to fit $\zeta(z)$, and the result is given in Table 1. We nevertheless have checked that the fitted envelope also well describes the wiggles of low-frequency models.

5. Expected constraints from *Euclid* primary probes

In this section, we show the results of the Fisher analysis for the cosmological parameters of interest corresponding to a flat Λ CDM,

$$\Theta_{\text{final}} = \{\Omega_{\text{m},0}, \Omega_{\text{b},0}, h, n_s, \sigma_8, \mathcal{A}_X, \omega_X, \phi_X\}, \quad (51)$$

after marginalisation over spectroscopic and photometric nuisance parameters. We compute the spectroscopic galaxy clustering (GC_{sp}), the photometric galaxy clustering (GC_{ph}), the weak lensing (WL), and the cross-correlation between the two photometric probes (XC) in two configurations: a pessimistic setting and an optimistic one. For the pessimistic setting, for GC_{sp} we have $k_{\text{max}} = 0.25 h \text{Mpc}^{-1}$, for GC_{ph} and XC we have $\ell_{\text{max}} = 750$, and for WL we have $\ell_{\text{max}} = 1500$. In addition, we impose a cut in redshift of $z < 0.9$ to GC_{ph} to limit any possible cross-correlation between spectroscopic and photometric data. For the optimistic setting, we extend GC_{sp} to $k_{\text{max}} = 0.30 h \text{Mpc}^{-1}$, GC_{ph} and XC

Table 2. Fisher-forecast 68.3% CL marginalised uncertainties on cosmological and primordial feature parameters, relative to their corresponding fiducial values.

LIN $\omega_{\text{lin}} = 10$								
	$\Omega_{\text{m},0}$	$\Omega_{\text{b},0}$	h	n_s	σ_8	\mathcal{A}_{lin}	ω_{lin}	ϕ_{lin}
Pessimistic setting								
GC _{sp} ($k_{\text{max}} = 0.25 h \text{ Mpc}^{-1}$)	1.2%	1.7%	1.4%	1.5%	0.83%	23%	4.1%	0.11
WL+GC _{ph} +XC	0.83%	5.7%	4.0%	1.6%	0.39%	32%	5.7%	0.12
GC _{sp} +WL+GC _{ph} +XC ($z < 0.9$)	0.61%	1.3%	0.59%	0.70%	0.28%	21%	2.9%	0.083
Optimistic setting								
GC _{sp} ($k_{\text{max}} = 0.3 h \text{ Mpc}^{-1}$)	1.1%	1.6%	1.1%	1.3%	0.76%	23%	3.6%	0.10
WL+GC _{ph} +XC	0.27%	4.4%	2.5%	0.66%	0.13%	31%	2.8%	0.072
GC _{sp} +WL+GC _{ph} +XC	0.23%	1.1%	0.45%	0.28%	0.11%	18%	1.2%	0.047
LOG $\omega_{\text{log}} = 10$								
	$\Omega_{\text{m},0}$	$\Omega_{\text{b},0}$	h	n_s	σ_8	\mathcal{A}_{log}	ω_{log}	ϕ_{log}
Pessimistic setting								
GC _{sp} ($k_{\text{max}} = 0.25 h \text{ Mpc}^{-1}$)	1.1%	1.8%	1.4%	1.5%	0.82%	25%	4.7%	0.053
WL+GC _{ph} +XC	0.83%	5.7%	4.0%	1.6%	0.38%	32%	5.7%	0.12
GC _{sp} +WL+GC _{ph} +XC ($z < 0.9$)	0.61%	1.4%	0.59%	0.71%	0.28%	22%	2.4%	0.044
Optimistic setting								
GC _{sp} ($k_{\text{max}} = 0.3 h \text{ Mpc}^{-1}$)	1.1%	1.8%	1.1%	1.3%	0.76%	25%	4.7%	0.052
WL+GC _{ph} +XC	0.27%	4.4%	2.5%	0.66%	0.13%	31%	2.8%	0.072
GC _{sp} +WL+GC _{ph} +XC	0.23%	1.1%	0.46%	0.28%	0.11%	18%	1.1%	0.035

Notes. We show results for LIN and LOG models in the pessimistic and optimistic settings, using *Euclid* observations GC_{sp}, WL+GC_{ph}+XC, and their combination.

to $\ell_{\text{max}} = 3000$, and WL to $\ell_{\text{max}} = 5000$, without imposing any redshift cut to GC_{ph}.

We start by presenting results for a fiducial scenario with $\mathcal{A}_X = 0.01$, $\omega_X = 10$, and $\phi_X = 0$. The marginalised uncertainties on the cosmological parameters and primordial feature parameters, percentages relative to the corresponding fiducial values, are collected in Table 2 for the pessimistic (top panel) and optimistic (bottom panel) settings. The marginalised 68.3% and 95.5% confidence level (CL) contours for the primordial feature parameters are shown in Fig. 4. For the fiducial value parameters, uncertainties on the amplitude of the primordial feature oscillations are dominated by GC_{sp} measurements resulting in $\mathcal{A}_{\text{lin}} = 0.0100 \pm 0.0023$ (± 0.0023) and $\mathcal{A}_{\text{log}} = 0.0100 \pm 0.0025$ (± 0.0025) at a 68.3% CL for the pessimistic (optimistic) setting. Combining GC_{sp} with the combination of photometric information, i.e. WL+GC_{ph}+XC, we find $\mathcal{A}_{\text{lin}} = 0.0100 \pm 0.0021$ (± 0.0018) and $\mathcal{A}_{\text{log}} = 0.0100 \pm 0.0022$ (± 0.0018) at a 68.3% CL for the pessimistic (optimistic) setting.

For GC_{sp}, bounds on the primordial amplitude parameter \mathcal{A}_X strongly depend on the primordial frequency value ω_X ; see Huang et al. (2012); Ballardini et al. (2016); Slosar et al. (2019); Beutler et al. (2019); Ballardini et al. (2020). Low frequencies, lower than the BAO one, leave a broad modification on the matter power spectrum and are expected to be better constrained by CMB measurements. On the other hand, the imprint from high-frequency primordial oscillations is smoothed by projection effects on the observed matter power spectrum. Moreover, for the linear model the uncertainties for frequencies around the BAO frequency, i.e. $\log_{10} \omega_{\text{lin}} \sim 0.87$, are degraded. For the combination of photometric probes, bounds on the primordial amplitude parameter \mathcal{A}_X are smoothed by projection effects in angular space and high-frequency primordial oscillations are severely washed out on the observed matter power spectrum. On the other hand, uncertainties for frequencies around the BAO scale and lower frequencies are tighter compared to the results from GC_{sp}.

This represents an important result considering the lower accuracy of the PT predictions for low frequencies.

In Fig. 5, we show the uncertainties at a 68.3% CL for different values of the primordial frequency $\log_{10} \omega_X$ within the range (0.1, 2.1). The combination of the spectroscopic and photometric probes allows us to reach uncertainties of 0.002–0.003 on the primordial feature amplitude for the entire range of frequencies.

The nonlinear reconstruction described in Sect. 4.4 applied to GC_{sp} reduces significantly the uncertainties on the feature amplitude, going from $\sigma(\mathcal{A}_{\text{lin}}) = 0.0023$ (0.0023) at a 68.3% CL for the pessimistic (optimistic) setting to $\sigma(\mathcal{A}_{\text{lin}}) = 0.0014$ (0.0013), and going from $\sigma(\mathcal{A}_{\text{log}}) = 0.0025$ (0.0025) to $\sigma(\mathcal{A}_{\text{log}}) = 0.0016$ (0.0012). Combining with the photometric probes, we find $\sigma(\mathcal{A}_{\text{lin}}) = 0.0014$ (0.0012) at a 68.3% CL and $\sigma(\mathcal{A}_{\text{log}}) = 0.0015$ (0.0012) for the pessimistic (optimistic) setting, compared with $\sigma(\mathcal{A}_{\text{lin}}) = 0.0021$ (0.0018) at a 68.3% CL and $\sigma(\mathcal{A}_{\text{log}}) = 0.0022$ (0.0018) for the same settings without reconstruction. We also note that in the analysis here k_{max} is set to be 0.25–0.30 $h \text{ Mpc}^{-1}$, while in Li et al. (2022) $k_{\text{max}} = 0.50 h \text{ Mpc}^{-1}$ is used.

6. Power spectrum and bispectrum combination

In this section, we present the forecast results on primordial features by combining the power spectrum and bispectrum signals. The presence of a sharp feature in the inflaton potential violates the slow-roll evolution, generating a linearly spaced oscillating primordial bispectrum. In this case the primordial bispectrum can be characterised by the standard amplitude parameter $f_{\text{NL}}^{\text{lin}}$, the phase ϕ_{lin}^B , and the frequency ω_{lin} , and it is given by (Chen et al. 2007, 2008)

$$B_{\Phi}^{\text{lin}}(k_1, k_2, k_3) = f_{\text{NL}}^{\text{lin}} \frac{6A^2}{k_1^2 k_2^2 k_3^2} \sin \left[\omega_{\text{lin}} \frac{K}{k_*} + 2\pi\phi_{\text{lin}}^B \right], \quad (52)$$

where $K = k_1 + k_2 + k_3$ and $A = 9/25(2\pi^2)k_*^{1-n_s}A_s$ is the normalisation parameter of $P_{\Phi} = A/k^{(4-n_s)}$.

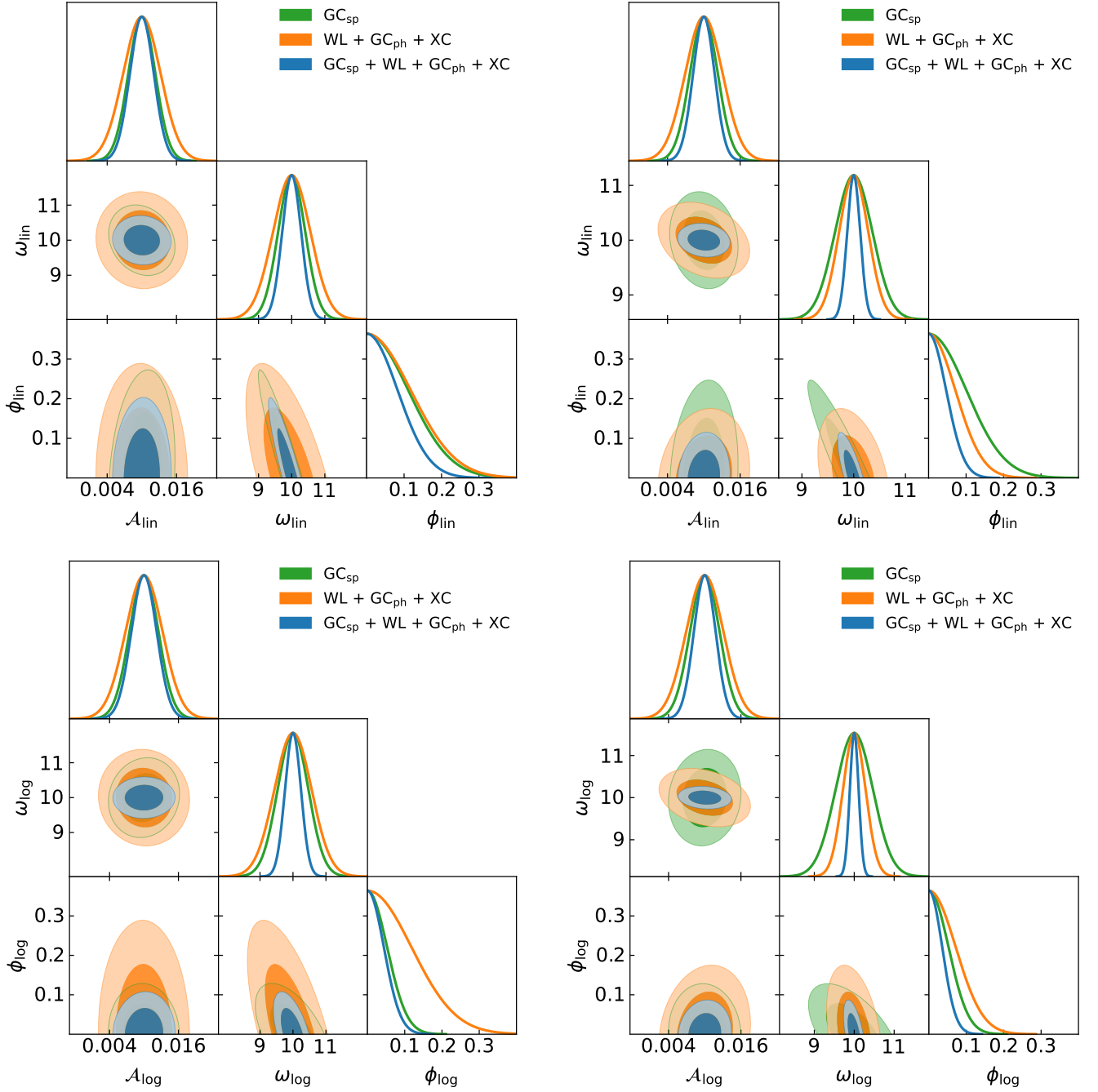


Fig. 4. Fisher-forecast marginalised two-dimensional contours and one-dimensional probability distribution functions from *Euclid* on the primordial feature parameters for the LIN model with $\omega_{\text{lin}} = 10$ (top panels) and the LOG model with $\omega_{\text{log}} = 10$ (bottom panels). Left (right) panels correspond to the pessimistic (optimistic) setting for GC_{sp} (green), $\text{WL} + \text{GC}_{\text{ph}} + \text{XC}$ (orange), and their combination (blue).

A periodically modulated inflaton potential leads to resonances in the inflationary fluctuations with logarithmically-spaced oscillations (Chen et al. 2008). This generates oscillatory features in the primordial power spectrum (see Sect. 4) and bispectrum (Flauger et al. 2010; Hannestad et al. 2010; Barnaby et al. 2012). In this case, the primordial bispectrum is given by (Chen 2010)

$$B_{\Phi}^{\text{log}}(k_1, k_2, k_3) = f_{\text{NL}}^{\text{log}} \frac{6A^2}{k_1^2 k_2^2 k_3^2} \sin \left[\omega_{\text{log}} \ln \left(\frac{K}{k_*} \right) + 2\pi\phi_{\text{log}}^B \right], \quad (53)$$

where ϕ_{log}^B and $f_{\text{NL}}^{\text{log}}$ are the phase and the amplitude, respectively, of the generated logarithmic features on the primordial bispectrum. Note that here we assume the frequency of the primordial feature bispectrum to be the same as in the case of the power spectrum (see Sect. 4.1)

The redshift space model, for the galaxy bispectrum, is given after considering non-Gaussian initial conditions, as dictated by the oscillatory features, up to second order terms in RSD, bias, and matter expansions. The tree-level modelling can be written

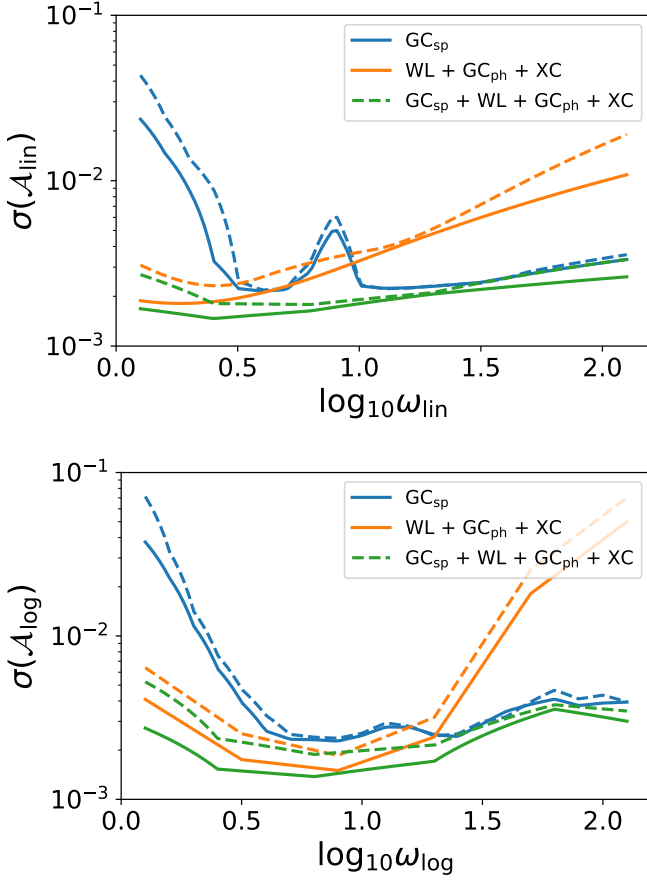


Fig. 5. Marginalised uncertainties on \mathcal{A}_X as a function of the primordial frequency ω_X for the LIN model (top panel) and the LOG model (bottom panel). We show uncertainties for GC_{sp} (blue), $\text{WL} + \text{GC}_{\text{ph}} + \text{XC}$ (orange), and their combination (green). Dashed (solid) curves correspond to the pessimistic (optimistic) setting.

as

$$P_g(\mathbf{k}, z) = D^P(\mathbf{k}, z) Z_1^2(\mathbf{k}, z) P^{\text{lin}}(\mathbf{k}, z) + P_\varepsilon(z), \quad (54)$$

$$\begin{aligned} B_g(\mathbf{k}_1, \mathbf{k}_2, \mathbf{k}_3, z) &= D^B(\mathbf{k}_1, \mathbf{k}_2, \mathbf{k}_3, z) \\ &\times \left[Z_1(\mathbf{k}_1, z) Z_1(\mathbf{k}_2, z) Z_1(\mathbf{k}_3, z) B_I(\mathbf{k}_1, \mathbf{k}_2, \mathbf{k}_3, z) \right. \\ &+ 2Z_1(\mathbf{k}_1, z) Z_1(\mathbf{k}_2, z) Z_2(\mathbf{k}_1, \mathbf{k}_2, z) P_{\text{lin}}(\mathbf{k}_1, z) P_{\text{lin}}(\mathbf{k}_2, z) + 2 \text{ perm} \left. \right] \\ &+ 2P_{\varepsilon\varepsilon_\delta} [Z_1(\mathbf{k}_1, z) P_{\text{lin}}(\mathbf{k}_1, z) + 2 \text{ perm}] + B_\varepsilon, \end{aligned} \quad (55)$$

where the linearly propagated primordial oscillatory bispectrum is

$$B_I(\mathbf{k}_1, \mathbf{k}_2, \mathbf{k}_3, z) = M(k_1, z) M(k_2, z) M(k_3, z) B_\Phi^X(k_1, k_2, k_3, z) \quad (56)$$

with B_Φ^X given by Eqs. (52) and (53) for the linear and logarithmic oscillations, respectively. The redshift space kernels are given by

$$Z_1(\mathbf{k}_i, z) = b_1(z) + f\mu_i^2, \quad (57)$$

$$\begin{aligned} Z_2(\mathbf{k}_i, \mathbf{k}_j, z) &= b_1(z) F_2(\mathbf{k}_i, \mathbf{k}_j) + f(z) \mu_{ij}^2 G_2(\mathbf{k}_i, \mathbf{k}_j) + \frac{b_2(z)}{2} \\ &+ \frac{b_{s^2}(z)}{2} S_2(\mathbf{k}_i, \mathbf{k}_j) + \frac{f(z) \mu_i \mu_j k_{ij}}{2} \left[\frac{\mu_i}{k_i} Z_1(\mathbf{k}_j, z) + \frac{\mu_j}{k_j} Z_1(\mathbf{k}_i, z) \right], \end{aligned} \quad (58)$$

where $\mu_i = \mathbf{k}_i \cdot \hat{z}/k_i$ is the cosine of the angle between the wave vector \mathbf{k}_i and the line of sight, $\mu = \mu_1 + \dots + \mu_n$, and $k = |\mathbf{k}_1 + \dots + \mathbf{k}_n|$. Specifically $\mu_{12} = (\mu_1 k_1 + \mu_2 k_2)/k_{12}$ and $k_{12}^2 = (\mathbf{k}_1 + \mathbf{k}_2)^2$. The kernels $F_2(\mathbf{k}_i, \mathbf{k}_j)$ and $G_2(\mathbf{k}_i, \mathbf{k}_j)$ are the second-order symmetric PT kernels (Bernardeau et al. 2002), while $S_2(\mathbf{k}_1, \mathbf{k}_2) = (\mathbf{k}_1 \cdot \mathbf{k}_2)^2 / (k_1^2 k_2^2) - 1/3$ is the tidal kernel (McDonald & Roy 2009; Baldauf et al. 2012). The second-order tidal field bias term, following the convention of (Baldauf et al. 2012), is given by $b_{s^2}(z) = -4[b_1(z) - 1]/7$. The redshift-space bispectrum is characterised by five variables: three to define the triangle shape (the sides k_1, k_2, k_3) and two that characterise the orientation of the triangle relative to the line of sight, i.e. $B_g(\mathbf{k}_1, \mathbf{k}_2, \mathbf{k}_3, z) = B_g(k_1, k_2, k_3, \mu_1, \phi, z)$. The forecasts presented here use the information of the bispectrum monopole obtained after taking the average over all angles.

Note that the presence of an oscillatory primordial bispectrum generates a scale-dependent correction to the linear bias, in a similar manner to the local primordial non-Gaussian case (see Karagiannis et al. 2018, for discussions). Cabass et al. (2018) show that the scale-dependent correction oscillates with scale with an envelope similar to that of equilateral primordial non-Gaussianity (PNG) (see Schmidt & Kamionkowski 2010; Scoccimarro et al. 2012; Schmid & Hui 2013; Assassi et al. 2015, for a discussion), while their findings indicate that the amplitude of such a term is very small to be detected by upcoming surveys. Therefore, we do not consider the scale-dependent terms in our analysis and exclude them from the expressions of the redshift kernels presented above. This means that the degeneracy between the scale-dependent bias coefficient and the primordial bispectrum amplitude (f_{NL}^X), shown in Barreira (2020), does not affect our forecasts.

The multiplicative factors $D^P(\mathbf{k}, z)$ and $D^B(\mathbf{k}_1, \mathbf{k}_2, \mathbf{k}_3, z)$, which incorporate errors on redshift measurements and FOG effect, are $D^P(\mathbf{k}, z) = \exp[-k\mu(\sigma_p^2(z) + \sigma_r^2(z))]$ and $D^B(\mathbf{k}_1, \mathbf{k}_2, \mathbf{k}_3, z) = \exp[-(k_1^2 \mu_1^2 + k_2^2 \mu_2^2 + k_3^2 \mu_3^2)(\sigma_p^2(z) + \sigma_r^2(z))/2]$ for the power spectrum and bispectrum, respectively (see Sect. 3.1 for details). The fiducial values of the stochastic terms in Eqs. (54) and (55) are taken to be those predicted by Poisson statistics (Schmidt 2016; Desjacques et al. 2018), i.e. $P_\varepsilon = 1/\bar{n}_g$, $P_{\varepsilon\varepsilon_\delta} = b_1/(2\bar{n}_g)$, and $B_\varepsilon = 1/\bar{n}_g^2$.

The AP effect is taken into account also for the bispectrum similar to the power spectrum case (see Sect. 3.1). The observed bispectrum is thus given by (see Karagiannis et al. 2022)

$$\begin{aligned} B_g^{\text{obs}}(k_{\text{ref},1}, k_{\text{ref},2}, k_{\text{ref},3}, \mu_{\text{ref},1}, \phi; z) \\ = \frac{1}{q_{\parallel}^2 q_{\perp}^4} B_g(k(k_{\text{ref},1}), k(k_{\text{ref},2}), k(k_{\text{ref},3}), \mu(\mu_{\text{ref},1}), \phi; z). \end{aligned} \quad (59)$$

Here we again use the Fisher matrix formalism to produce forecasts on the model parameters that control the primordial oscillations. The Fisher matrix of the redshift galaxy power spectrum is given by Eq. (12), while for the bispectrum the Fisher matrix for one redshift bin z_i is given by

$$\begin{aligned} F_{\alpha\beta}^B(z_i) &= \frac{1}{4\pi} \sum_{k_1, k_2, k_3} \int_{-1}^1 d\mu_1 \int_0^{2\pi} d\phi \frac{1}{\Delta B^2(\mathbf{k}_1, \mathbf{k}_2, \mathbf{k}_3, z_i)} \\ &\times \frac{\partial B_g^{\text{obs}}(\mathbf{k}_1, \mathbf{k}_2, \mathbf{k}_3, z_i)}{\partial p_\alpha} \frac{\partial B_g^{\text{obs}}(\mathbf{k}_1, \mathbf{k}_2, \mathbf{k}_3, z_i)}{\partial p_\beta}, \end{aligned} \quad (60)$$

where the sum over triangles has $k_{\text{min}} \leq k_3 \leq k_2 \leq k_1 \leq k_{\text{max}}$, and k_1, k_2 and k_3 satisfy the triangle inequality. The bin size Δk is

taken to be the fundamental frequency of the survey, $k_f = 2\pi/L$, where for simplicity we approximate the survey volume as a cube, $L = V_{\text{survey}}^{1/3}$. The k mode is binned with a bin size of Δk , and here we consider $\Delta k = k_f$, between its minimum and maximum values $k_{\min} = k_f$ and k_{\max} . Gaussian approximation is used for the covariance of bispectrum, i.e. the off-diagonal terms are considered to be zero.⁷ The variance for the bispectrum is then (Sefusatti et al. 2007)

$$\Delta B^2(\mathbf{k}_1, \mathbf{k}_2, \mathbf{k}_3, z) = s_{123} \pi k_f(z)^3 \frac{P_g(\mathbf{k}_1, z) P_g(\mathbf{k}_2, z) P_g(\mathbf{k}_3, z)}{k_1 k_2 k_3 \Delta k(z)^3}, \quad (61)$$

where $s_{123} = 6, 2, 1$ for equilateral, isosceles, and non-isosceles triangles, respectively. In addition, for degenerate configurations, i.e. $k_i = k_j + k_m$, the bispectrum variance should be multiplied by a factor of 2 (Chan & Blot 2017; Desjacques et al. 2018). We use the Fisher matrix of Eq. (60) to generate bispectrum forecasts on the parameters of interest

$$\Theta_{\text{final}}^B = \left\{ \Omega_{m,0}, \Omega_{b,0}, h, n_s, \sigma_8, A_X, \omega_X, \phi_X, f_{\text{NL}}^X, \phi_X^B \right\}. \quad (62)$$

The initial parameter vector considers all the parameters of the bispectrum tree-level modelling (i.e. cosmological parameters, biases, AP parameters, growth rate, and FOG amplitudes) to be free, and after marginalisation we derive the constraints for Θ_{final}^B . The forecasted marginalised 1σ errors on the feature model parameters, coming from the spectroscopic galaxy clustering, are presented in Table 3.

The galaxy bispectrum is capable of providing constraints not only on the feature parameters related to the primordial bispectrum but also on those controlling the primordial power spectrum feature model. The latter is due to the $P_{\text{lin}}(k_i)P_{\text{lin}}(k_j)$ terms that are present at tree level in the galaxy bispectrum (55) and can provide constraints equivalent to or even better than the galaxy power spectrum, especially in the case of a high k_{\max} . This can be seen in Table 3, where adding the power spectrum to the bispectrum improves the forecasts by a few percent. This highlights the importance of a bispectrum analysis for the type of feature models discussed in this work. On the other hand, the sole contribution to the constraints on the f_{NL}^X and ϕ_X^B feature parameters is the primordial component B_l of the galaxy bispectrum, justifying the less rigorous forecasts presented here.

7. Combination with CMB data

Future CMB polarisation data from ground-based experiments, such as Simons Observatory (Ade et al. 2019) and CMB-S4 (Abazajian et al. 2019), and satellites, such as LiteBIRD (LiteBIRD Collaboration: Allys et al. 2023), will be able to reduce the uncertainties on the PPS, in particular in the presence of oscillatory signals. Indeed, E-mode polarisation is sourced by velocity gradient (scattering only) leading to sharper transfer functions compared to the temperature ones helping to characterise primordial features in the PPS; see Mortonson et al. (2009); Miranda et al. (2015); Ballardini et al. (2016); Finelli et al. (2018); Hazra et al. (2018); Braglia et al. (2023).

⁷ Neglecting the off-diagonal terms in the bispectrum covariance can have a significant impact on the constraints on primordial features, since these contributions are important even on large scales for squeezed triangles (Gualdi & Verde 2020; Biagetti et al. 2022; Flöss et al. 2023). Considering the analytic expression of the full bispectrum covariance is left for future work.

Table 3. Fisher-forecast 68.3% CL marginalised uncertainties on primordial feature parameters, relative to their corresponding fiducial values, using *Euclid* GC_{sp} bispectrum.

	P	B	P+B
Pessimistic setting ($k_{\max} = 0.25 h \text{ Mpc}^{-1}$)			
A_{lin}	23%	16%	13%
ω_{lin}	4.1%	2.1%	1.7%
ϕ_{lin}	0.11	-	0.049
$f_{\text{NL}}^{\text{lin}}$	-	31	31
ϕ_{lin}^B	-	4.9	4.9
A_{log}	25%	17%	13%
ω_{log}	4.7%	2.9%	2.4%
ϕ_{log}	0.053	-	0.026
$f_{\text{NL}}^{\text{log}}$	-	33	32
ϕ_{log}^B	-	5.2	5.1
Optimistic setting ($k_{\max} = 0.3 h \text{ Mpc}^{-1}$)			
A_{lin}	23%	12%	11%
ω_{lin}	3.6%	1.4%	1.2%
ϕ_{lin}^P	0.10	-	0.039
$f_{\text{NL}}^{\text{lin}}$	-	29	29
ϕ_{lin}^B	-	4.6	4.6
A_{log}	25%	13%	11%
ω_{log}	4.7%	2.2%	2.0%
ϕ_{log}	0.052	-	0.023
$f_{\text{NL}}^{\text{log}}$	-	30	30
ϕ_{log}^B	-	4.8	4.8

Notes. We show results for LIN and LOG models in the pessimistic and optimistic settings in the case, using the *Euclid* GC_{sp} bispectrum and the joint power spectrum+bispectrum signal.

We consider the information available in the CMB data by using power spectra from temperature, E-mode polarisation, and CMB lensing in combination with *Euclid* observations. We do not consider B-mode polarisation since it does not add information for the specific models examined here. We also neglect the cross-spectra between CMB fields and *Euclid* primary probes; see *Euclid* Collaboration: Ilić et al. (2022) for a complete characterisation and quantification of the importance of cross-correlation between CMB and *Euclid* measurements. Following *Euclid* Collaboration: Ilić et al. (2022), we consider three CMB experiments: *Planck*-like, Simons Observatory (SO), and CMB-S4. Noise curves correspond to isotropic noise deconvolved with instrumental beam (Knox 1995)

$$\mathcal{N}_\ell^X = w_X^{-1} b_\ell^{-2}, \quad b_\ell = \exp \left[-\ell(\ell + 1) \theta_{\text{FWHM}}^2 / (16 \ln 2) \right], \quad (63)$$

where θ_{FWHM} is the full-width-at-half-maximum (FWHM) of the beam, w_T and w_E are the inverse square of the detector noise levels for temperature and polarisation, respectively. CMB lensing noise is reconstructed through minimum-variance estimator for the lensing potential using quicklens code;⁸ see Okamoto & Hu (2003).

⁸ <https://github.com/dhanson/quicklens>

For the *Planck*-like experiment, we use an effective sensitivity in order to reproduce the *Planck* 2018 results for the Λ CDM model (Planck Collaboration: Aghanim et al. 2020b) avoiding the complexity of the real-data likelihood (Planck Collaboration: Aghanim et al. 2020c). We use noise specifications corresponding to in-flight performances of the 143 GHz channel of the high-frequency instrument (HFI) (Planck Collaboration: Aghanim et al. 2020a) with a sky fraction $f_{\text{sky}} = 0.7$ and a multipole range for temperature and polarisation from $\ell_{\text{min}} = 2$ to $\ell_{\text{max}} = 1500$. The E-mode polarisation noise is inflated by a factor of 8 to reproduce the uncertainty of the optical depth parameter τ ; see Bermejo-Climent et al. (2021). Finally, CMB lensing is obtained by combining the 143 GHz and 217 GHz HFI channels assuming a conservative multipole range of 8–400. For the CMB, we also consider the optical depth at reionisation τ and then we marginalise over it before combining the CMB Fisher matrix with the *Euclid* ones.

For the SO-like experiment, we use noise curves provided by the SO collaboration in Ade et al. (2019) taking into account residuals and noises from component separation.⁹ We use spectra from $\ell_{\text{min}} = 40$ to $\ell_{\text{max}} = 3000$ for temperature and temperature-polarisation cross-correlation, and $\ell_{\text{max}} = 5000$ for E-mode polarisation. CMB lensing and temperature-lensing cross-correlation spectra cover the multipole range of 2–3000. The sky fraction considered is $f_{\text{sky}} = 0.4$. We complement the SO-like information with the *Planck*-like large-scale data in the multipole range of 2–40 in both temperature and polarisation.

For CMB-S4, we use noise sensitivities of $1 \mu\text{K}$ arcmin in temperature and $\sqrt{2} \mu\text{K}$ arcmin in polarisation, with resolution of $\theta_{\text{FWHM}} = 1$ arcmin. We assume data over the same multipole ranges of SO and with the same sky coverage.

Table 4. Fisher-matrix-based forecasted 68.3% CL marginalised uncertainties using *Euclid* in combination with the CMB.

	<i>Euclid</i> + <i>Planck</i> -like	<i>Euclid</i> + SO-like + <i>Planck</i> low- ℓ	<i>Euclid</i> + CMB-S4 + <i>Planck</i> low- ℓ
Pessimistic setting			
A_{lin}	18%	14%	12%
ω_{lin}	2.4%	1.2%	1.0%
ϕ_{lin}	0.066	0.046	0.043
A_{log}	17%	11%	7.9%
ω_{log}	1.9%	1.6%	1.5%
ϕ_{log}	0.048	0.036	0.033
Optimistic setting			
A_{lin}	16%	13%	12%
ω_{lin}	1.0%	0.92%	0.85%
ϕ_{lin}	0.042	0.038	0.037
A_{log}	15%	10%	7.6%
ω_{log}	1.1%	1.0%	0.98%
ϕ_{log}	0.037	0.027	0.024

Notes. We show results for LIN and LOG models in the pessimistic and optimistic settings in the case, relative to their corresponding fiducial values ($\mathcal{A}_X = 0.01$, $\omega_X = 10$, using *Euclid* (GC_{sp}+WL+GC_{ph}+XC) in combination with the CMB.

In Table 4, we show the marginalised uncertainties on the primordial feature parameters, percentage relative to the corresponding fiducial values, for the optimistic and pessimistic *Eu-*

⁹ We use version 3.1.0 available at https://github.com/simonsobs/so_noise_models.

clid + CMB combination. Uncertainties on the primordial feature amplitude improve by 15%–50% depending on the choice of *Euclid* settings and on the CMB experiment considered, for a frequency value of $\omega_X = 10$.

8. Conclusions

We have explored the constraining power of the future *Euclid* space mission for oscillatory primordial features in the primordial power spectrum (PPS) of density perturbations. We have considered two templates with undamped oscillations, i.e. with constant amplitude all over the PPS, one linearly and one logarithmically spaced in k space. We have used a common baseline set of parameters for both the templates with amplitude $\mathcal{A}_X = 0.01$, frequency $\omega_X = 10$, and phase $\phi_X = 0$, where $X = \{\text{lin}, \text{log}\}$.

Following previous studies for Λ CDM and simple extensions in Euclid Collaboration: Blanchard et al. (2020), we have calculated Fisher-matrix-based uncertainties from *Euclid* primary probes, i.e. spectroscopic galaxy clustering (GC_{sp}) and the combination of photometric galaxy clustering (GC_{ph}) and photometric weak lensing (WL); see Sect. 3. We have considered two sets of *Euclid* specifications: a pessimistic setting with $k_{\text{max}} = 0.25 h \text{Mpc}^{-1}$ for GC_{sp}, $\ell_{\text{max}} = 1500$ for WL, $\ell_{\text{max}} = 750$ for GC_{ph} and XC, and a cut in redshift of $z < 0.9$ to GC_{ph}; an optimistic setting with $k_{\text{max}} = 0.30 h \text{Mpc}^{-1}$ for GC_{sp}, $\ell_{\text{max}} = 5000$ for WL, and $\ell_{\text{max}} = 3000$ for GC_{ph} and XC.

We have modelled the nonlinear matter power spectrum with time-sliced perturbation theory predictions at leading order (Vasudevan et al. 2019; Beutler et al. 2019; Ballardini et al. 2020; Ballardini & Finelli 2022) calibrated on a set of N-body simulations from COLA (Tassev et al. 2013; Howlett et al. 2015) and GADGET (Springel et al. 2001; Springel 2005; Ballardini et al. 2020; Ballardini & Finelli 2022) for GC_{sp}; see Sect. 4.2. For modelling of the photometric probes we rely on HMCODE (Mead et al. 2016) to describe the broadband small-scale behaviour and on PT to describe the smearing of BAO and primordial features; see Sect. 4.2.

With the full set of probes, i.e. GC_{sp}+WL+GC_{ph}+XC, we have found that *Euclid* alone is able to constrain the amplitude of a primordial oscillatory feature with frequency $\omega_X = 10$ to $\mathcal{A}_X = 0.010 \pm 0.002$ at a 68.3% CL both in the pessimistic and optimistic settings; see Sect. 5 and Table 2. When we consider single *Euclid* probes these uncertainties depend strongly on the frequency (see Fig. 5) and are weakened for low and high frequencies. However, we have found robust constraints of 0.002–0.003 from the full combination of *Euclid* probes over the frequency range of $(1, 10^{2.1})$.

We have then considered further information available from *Euclid* measurements including a numerical reconstruction of nonlinear spectroscopic galaxy clustering (Beutler et al. 2019; Li et al. 2022) and the galaxy clustering bispectrum (Karagiannis et al. 2018); see Sect. 4.4 and Sect. 6, respectively. We have found $\mathcal{A}_{\text{lin}} = 0.0100 \pm 0.0014$ ($\mathcal{A}_{\text{log}} = 0.0100 \pm 0.0015$) in the pessimistic setting and $\mathcal{A}_{\text{lin}} = 0.0100 \pm 0.0012$ ($\mathcal{A}_{\text{log}} = 0.0100 \pm 0.0012$) in the optimistic setting, both at 68.3% CL, from GC_{sp} (rec)+WL+GC_{ph}+XC. This shows that reconstruction can potentially tighten the constraints on the primordial feature amplitude. Including the galaxy clustering bispectrum, we further tighten the uncertainties on the primordial feature amplitude to $\mathcal{A}_{\text{lin}} = 0.0100 \pm 0.0009$ ($\mathcal{A}_{\text{log}} = 0.0100 \pm 0.0009$) in the pessimistic setting and $\mathcal{A}_{\text{lin}} = 0.0100 \pm 0.0008$ ($\mathcal{A}_{\text{log}} = 0.0100 \pm 0.0008$) in the optimistic setting, both at 68.3% CL, from GC_{sp} (rec)+WL+GC_{ph}+XC+BS.

Finally, we have studied the combination of *Euclid* probes and the expected information from CMB experiments by adding (without including the cross-correlation) forecasted results from *Planck*, Simons Observatory (SO), and CMB-S4 following [Euclid Collaboration: Ilić et al. \(2022\)](#); see Sect. 7. Combining the Fisher matrix information from a SO-like experiment (complemented with a *Planck*-like one at low- ℓ) with the *Euclid* primary probes, we have found $\mathcal{A}_{\text{lin}} = 0.0100 \pm 0.0014$ ($\mathcal{A}_{\text{log}} = 0.0100 \pm 0.0011$) in the pessimistic setting and $\mathcal{A}_{\text{lin}} = 0.0100 \pm 0.0013$ ($\mathcal{A}_{\text{log}} = 0.0100 \pm 0.0010$) in the optimistic setting, both at 68.3% CL.

We summarise in Fig. 6 the comparison of *Euclid* measurements in combination with other non-primary sources of information. Our tightest uncertainties, combining all the sources of information expected from *Euclid* in combination with future CMB experiments, e.g SO complemented with *Planck* at low- ℓ , correspond to $\mathcal{A}_{\text{lin}} = 0.0100 \pm 0.0008$ at a 68.3% CL and to $\mathcal{A}_{\text{log}} = 0.0100 \pm 0.0008$ for GC_{sp} (PS rec + BS)+WL+GC_{ph}+XC+SO-like for both the pessimistic and the optimistic settings.

Our results highlight the power of *Euclid* measurements to constrain primordial feature signals helping us to reach a more complete picture of the physics of the early Universe and to improve over the current bounds on the primordial feature amplitude parameter \mathcal{A}_X . In addition, the expected observations from *Euclid* will allow us to scrutinise the primordial interpretation of some of the anomalies in the CMB temperature and polarisation angular power spectra corresponding to the following best-fits of *Planck* data ([Planck Collaboration: Aghanim et al. 2020b](#)): $\mathcal{A}_{\text{lin}} = 0.015$ and $\log_{10} \omega_{\text{lin}} = 1.05$ for the linear oscillations, $\mathcal{A}_{\text{log}} = 0.014$ and $\log_{10} \omega_{\text{log}} = 1.26$ for the logarithmic oscillations.

Acknowledgements. MBall acknowledges financial support from the INFN In-Dark initiative and from the COSMOS network (www.cosmosnet.it) through the ASI (Italian Space Agency) Grants 2016-24-H.0 and 2016-24-H.1-2018, as well as 2020-9-HH.0 (participation in LiteBIRD phase A). YA acknowledges support by the Spanish Research Agency (Agencia Estatal de Investigación)'s grant RYC2020-030193-I/AEI/10.13039/501100011033 and the European Social Fund (Fondo Social Europeo) through the Ramón y Cajal program within the State Plan for Scientific and Technical Research and Innovation (Plan Estatal de Investigación Científica y Técnica y de Innovación) 2017-2020, and by the Spanish Research Agency through the grant IFT Centro de Excelencia Severo Ochoa No CEX2020-001007-S funded by MCIN/AEI/10.13039/501100011033. DK was supported by the South African Radio Astronomy Observatory and the National Research Foundation (Grant No. 75415). BL is supported by the European Research Council (ERC) through a starting Grant (ERC-StG-716532 PUNCA), and the UK Science and Technology Facilities Council (STFC) Consolidated Grant No. ST/100162X/1 and ST/P000541/1. ZS acknowledges ITP institute funding from DFG project 456622116 and IRAP lab support. DS acknowledges financial support from the Fondecyt Regular project number 1200171. MBald acknowledges support by the project 'Combining Cosmic Microwave Background and Large Scale Structure data: an Integrated Approach for Addressing Fundamental Questions in Cosmology', funded by the MIUR Progetti di Ricerca di Rilevante Interesse Nazionale (PRIN) Bando 2017 - grant 2017YJYZAH. GCH acknowledges support through the ESA research fellowship programme. HAW acknowledges support from the Research Council of Norway through project 325113. MV acknowledges partial financial support from the INFN PD51 IN-DARK grant and from the agreement ASI-INAF n.2017-14-H.0. Part of the N-body simulations presented in this work were obtained on the Ullysses super-computer at SISSA. JJ acknowledges support by the Swedish Research Council (VR) under the project 2020-05143 - 'Deciphering the Dynamics of Cosmic Structure'. GL acknowledges support by the ANR BIG4 project, grant ANR-16-CE23-0002 of the French Agence Nationale de la Recherche. AA, JJ, and GL acknowledge the support of the Simons Collaboration on "Learning the Universe". DP acknowledges financial support by agreement n. 2020-9-HH.0 ASI-UniRM2. JV was supported by Ruth och Nils-Erik Stenbäcks Stiftelse. The Euclid Consortium acknowledges the European Space Agency and a number of agencies and institutes that have supported the development of *Euclid*, in particular the Academy of Finland, the Agenzia Spaziale Italiana, the Belgian Science Policy, the Canadian Euclid Consortium, the French Centre National d'Etudes Spatiales, the Deutsches Zentrum für Luft- und Raumfahrt, the Danish Space Research

Institute, the Fundação para a Ciência e a Tecnologia, the Ministerio de Ciencia e Innovación, the National Aeronautics and Space Administration, the National Astronomical Observatory of Japan, the Nederlandse Onderzoeksschool Voor Astronomie, the Norwegian Space Agency, the Romanian Space Agency, the State Secretariat for Education, Research and Innovation (SERI) at the Swiss Space Office (SSO), and the United Kingdom Space Agency. A complete and detailed list is available on the *Euclid* web site (<http://www.euclid-ec.org>).

References

- Abazajian, K., Addison, G., Adshead, P., et al. 2019, arXiv e-prints, arXiv:1907.04473
- Achúcarro, A., Atal, V., Hu, B., Ortiz, P., & Torrado, J. 2014, *Phys. Rev. D*, 90, 023511
- Achúcarro, A., Biagetti, M., Braglia, M., et al. 2022, arXiv e-prints, arXiv:2203.08128
- Achúcarro, A., Gong, J.-O., Hardeman, S., Palma, G. A., & Patil, S. P. 2011, *J. Cosmology Astropart. Phys.*, 2011, 030
- Achúcarro, A., Gong, J.-O., Hardeman, S., Palma, G. A., & Patil, S. P. 2012, *Journal of High Energy Physics*, 2012, 66
- Adams, J., Cresswell, B., & Easther, R. 2001, *Phys. Rev. D*, 64, 123514
- Ade, P., Aguirre, J., Ahmed, Z., et al. 2019, *J. Cosmology Astropart. Phys.*, 2019, 056
- Albrecht, A. & Steinhardt, P. J. 1982, *Phys. Rev. Lett.*, 48, 1220
- Alcock, C. & Paczynski, B. 1979, *Nature*, 281, 358
- Amendola, L., Appleby, S., Avgoustidis, A., et al. 2018, *Living Reviews in Relativity*, 21, 2
- Ansari Fard, M. & Baghran, S. 2018, *J. Cosmology Astropart. Phys.*, 2018, 051
- Antony, A., Finelli, F., Hazra, D. K., & Shafieloo, A. 2023, *Phys. Rev. Lett.*, 130, 111001
- Assasi, V., Baumann, D., & Schmidt, F. 2015, *J. Cosmology Astropart. Phys.*, 12, 043
- Baldauf, T., Mirbabayi, M., Simonović, M., & Zaldarriaga, M. 2015, *Phys. Rev. D*, 92, 043514
- Baldauf, T., Seljak, U., Desjacques, V., & McDonald, P. 2012, *Phys. Rev. D*, 86, 083540
- Ballardini, M. 2019, *Physics of the Dark Universe*, 23, 100245
- Ballardini, M. & Finelli, F. 2022, *J. Cosmology Astropart. Phys.*, 2022, 083
- Ballardini, M., Finelli, F., Fedeli, C., & Moscardini, L. 2016, *J. Cosmology Astropart. Phys.*, 2016, 041
- Ballardini, M., Finelli, F., Maartens, R., & Moscardini, L. 2018, *J. Cosmology Astropart. Phys.*, 2018, 044
- Ballardini, M., Finelli, F., Marulli, F., Moscardini, L., & Veropalumbo, A. 2023, *Phys. Rev. D*, 107, 043532
- Ballardini, M., Murgia, R., Baldi, M., Finelli, F., & Viel, M. 2020, *J. Cosmology Astropart. Phys.*, 2020, 030
- Barnaby, N., Pajer, E., & Peloso, M. 2012, *Phys. Rev. D*, 85, 023525
- Barreira, A. 2020, *J. Cosmology Astropart. Phys.*, 2020, 031
- Bartolo, N., Cannone, D., & Matarrese, S. 2013, *J. Cosmology Astropart. Phys.*, 2013, 038
- Benetti, M. 2013, *Phys. Rev. D*, 88, 087302
- Bermejo-Climent, J. R., Ballardini, M., Finelli, F., et al. 2021, *Phys. Rev. D*, 103, 103502
- Bernardeau, F., Colombi, S., Gaztañaga, E., & Scoccimarro, R. 2002, *Phys. Rep.*, 367, 1
- Beutler, F., Biagetti, M., Green, D., Slosar, A., & Wallisch, B. 2019, *Physical Review Research*, 1, 033209
- Bezrukov, F. & Shaposhnikov, M. 2008, *Physics Letters B*, 659, 703
- Biagetti, M., Castiblanco, L., Noreña, J., & Sefusatti, E. 2022, *J. Cosmology Astropart. Phys.*, 2022, 009
- Birkin, J., Li, B., Cautun, M., & Shi, Y. 2019, *MNRAS*, 483, 5267
- Blas, D., Garny, M., Ivanov, M. M., & Sibiryakov, S. 2016a, *J. Cosmology Astropart. Phys.*, 2016, 052
- Blas, D., Garny, M., Ivanov, M. M., & Sibiryakov, S. 2016b, *J. Cosmology Astropart. Phys.*, 2016, 028
- Boyle, A. & Komatsu, E. 2018, *J. Cosmology Astropart. Phys.*, 2018, 035
- Braglia, M., Chen, X., & Hazra, D. K. 2021, *J. Cosmology Astropart. Phys.*, 2021, 005
- Braglia, M., Chen, X., & Hazra, D. K. 2022a, *Phys. Rev. D*, 105, 103523
- Braglia, M., Chen, X., & Hazra, D. K. 2022b, *European Physical Journal C*, 82, 498
- Braglia, M., Chen, X., Kumar Hazra, D., & Pinol, L. 2023, *J. Cosmology Astropart. Phys.*, 2023, 014
- Brenier, Y., Frisch, U., Hénon, M., et al. 2003, *MNRAS*, 346, 501
- Burden, A., Percival, W. J., Manera, M., et al. 2014, *MNRAS*, 445, 3152
- Cañas-Herrera, G., Torrado, J., & Achúcarro, A. 2021, *Phys. Rev. D*, 103, 123531

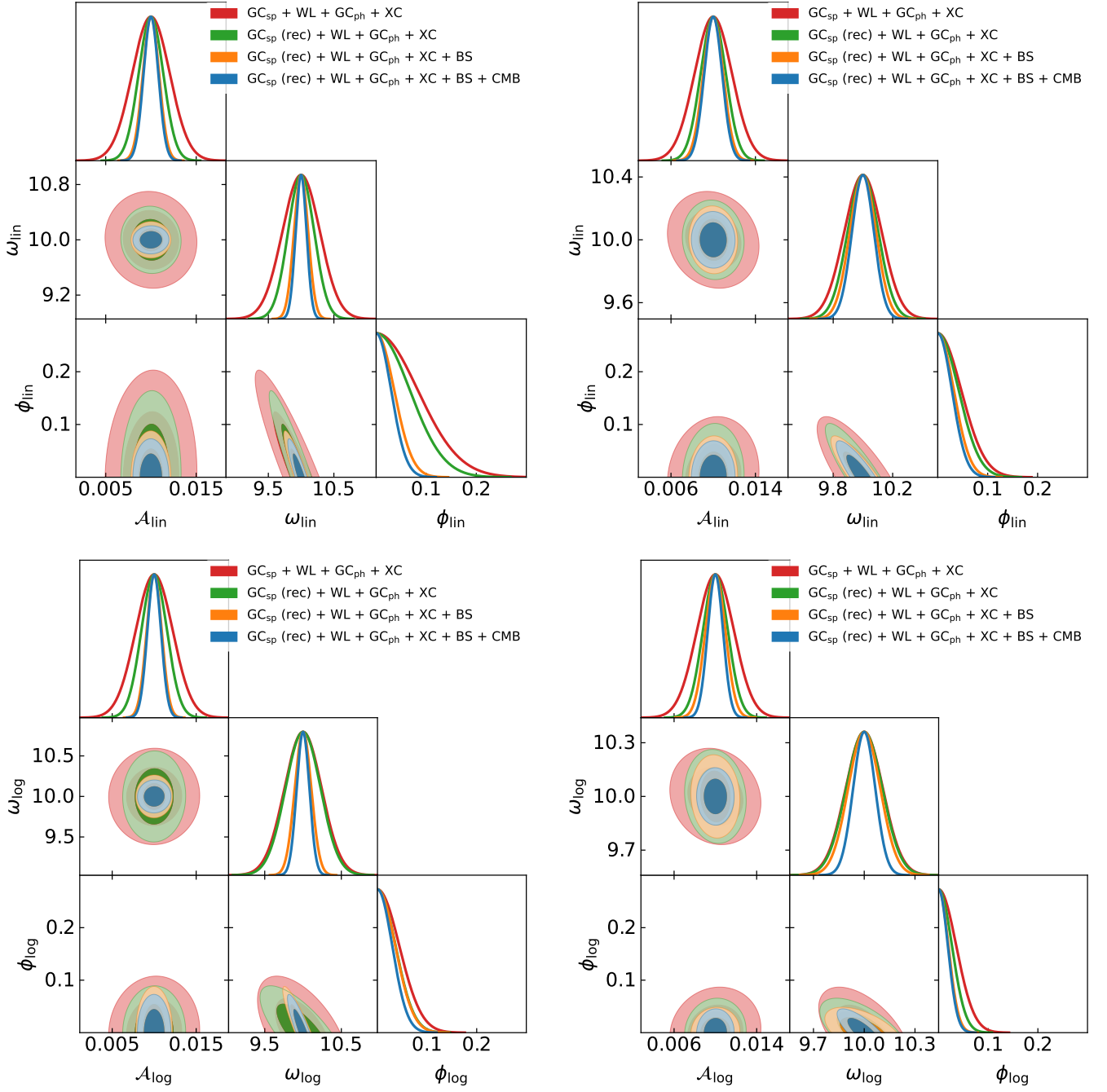


Fig. 6. Fisher-forecast marginalised two-dimensional contours and one-dimensional probability distribution functions from *Euclid* on the primordial feature parameters for the LIN model with $\omega_{\text{lin}} = 10$ (top panels) and the LOG model with $\omega_{\text{log}} = 10$ (bottom panels). Left (right) panels correspond to the pessimistic (optimistic) setting for $\text{GC}_{\text{sp}} + \text{WL} + \text{GC}_{\text{ph}} + \text{XC}$ (red), $\text{GC}_{\text{sp}} + \text{WL} + \text{GC}_{\text{ph}} + \text{XC}$ with numerical reconstruction of GC_{sp} (green), $\text{GC}_{\text{sp}}(\text{rec}) + \text{WL} + \text{GC}_{\text{ph}} + \text{XC}$ in combination with *Euclid* GC_{sp} bispectrum (orange), and their combination plus SO-like CMB (blue).

Cabass, G., Pajer, E., & Schmidt, F. 2018, *J. Cosmology Astropart. Phys.*, 2018, 003
Cannone, D., Bartolo, N., & Matarrese, S. 2014, *Phys. Rev. D*, 89, 127301
Cautun, M. C. & van de Weygaert, R. 2011, arXiv e-prints [arXiv:1105.0370]
Chan, K. C. & Blot, L. 2017, *Phys. Rev. D*, 96, 023528
Chen, S.-F., Vlah, Z., & White, M. 2020, *J. Cosmology Astropart. Phys.*, 2020, 035
Chen, X. 2010, *J. Cosmology Astropart. Phys.*, 2010, 003
Chen, X. 2012, *J. Cosmology Astropart. Phys.*, 2012, 038
Chen, X., Dvorkin, C., Huang, Z., Namjoo, M. H., & Verde, L. 2016a, *J. Cosmology Astropart. Phys.*, 2016, 014
Chen, X., Easter, R., & Lim, E. A. 2007, *J. Cosmology Astropart. Phys.*, 2007, 023

Chen, X., Easter, R., & Lim, E. A. 2008, *J. Cosmology Astropart. Phys.*, 2008, 010
Chen, X., Meerburg, P. D., & Münchmeyer, M. 2016b, *J. Cosmology Astropart. Phys.*, 2016, 023
Chen, X. & Namjoo, M. H. 2014, *Physics Letters B*, 739, 285
Cheung, C., Fitzpatrick, A. L., Kaplan, J., Senatore, L., & Creminelli, P. 2008, *Journal of High Energy Physics*, 3, 014
Chluba, J., Hamann, J., & Patil, S. P. 2015, *International Journal of Modern Physics D*, 24, 1530023
Covi, L., Hamann, J., Melchiorri, A., Slosar, A., & Sorbera, I. 2006, *Phys. Rev. D*, 74, 083509
Creminelli, P., Gleyzes, J., Simonović, M., & Vernizzi, F. 2014, *J. Cosmology Astropart. Phys.*, 2014, 051
Croce, M., Pueblas, S., & Scoccimarro, R. 2006, *MNRAS*, 373, 369

- Crocce, M. & Scoccimarro, R. 2008, *Phys. Rev. D*, 77, 023533
- Croft, R. A. C. & Gaztanaga, E. 1997, *MNRAS*, 285, 793
- Debono, I., Hazra, D. K., Shafieloo, A., Smoot, G. F., & Starobinsky, A. A. 2020, *MNRAS*, 496, 3448
- Desjacques, V., Jeong, D., & Schmidt, F. 2018, *Phys. Rep.*, 733, 1
- Domènech, G., Chen, X., Kamionkowski, M., & Loeb, A. 2020, *J. Cosmology Astropart. Phys.*, 2020, 005
- Domènech, G. & Kamionkowski, M. 2019, *J. Cosmology Astropart. Phys.*, 2019, 040
- Easther, R. & Flauger, R. 2014, *J. Cosmology Astropart. Phys.*, 2014, 037
- Eisenstein, D. J., Seo, H.-J., Sirko, E., & Spergel, D. N. 2007, *ApJ*, 664, 675
- Euclid Collaboration: Blanchard, A., Camera, S., Carbone, C., et al. 2020, *A&A*, 642, A191
- Euclid Collaboration: Ilić, S., Aghanim, N., Baccigalupi, C., et al. 2022, *A&A*, 657, A91
- Euclid Collaboration: Scaramella, R., Amiaux, J., Mellier, Y., et al. 2022, *A&A*, 662, A112
- Fang, X., Blazek, J. A., McEwen, J. E., & Hirata, C. M. 2017, *J. Cosmology Astropart. Phys.*, 2017, 030
- Fergusson, J. R., Gruetjen, H. F., Shellard, E. P. S., & Wallisch, B. 2015, *Phys. Rev. D*, 91, 123506
- Finelli, F., Bucher, M., Achúcarro, A., et al. 2018, *J. Cosmology Astropart. Phys.*, 2018, 016
- Flauger, R., McAllister, L., Pajer, E., Westphal, A., & Xu, G. 2010, *J. Cosmology Astropart. Phys.*, 2010, 009
- Flöss, T., Biagetti, M., & Meerburg, P. D. 2023, *Phys. Rev. D*, 107, 023528
- Freese, K., Frieman, J. A., & Olinto, A. V. 1990, *Phys. Rev. Lett.*, 65, 3233
- Gruppuso, A., Kitazawa, N., Mandolesi, N., Natoli, P., & Sagnotti, A. 2016, *Physics of the Dark Universe*, 11, 68
- Gruppuso, A. & Sagnotti, A. 2015, *International Journal of Modern Physics D*, 24, 1544008
- Gualdi, D. & Verde, L. 2020, *J. Cosmology Astropart. Phys.*, 2020, 041
- Guth, A. H. 1981, *Phys. Rev. D*, 23, 347
- Hada, R. & Eisenstein, D. J. 2018, *MNRAS*, 478, 1866
- Hada, R. & Eisenstein, D. J. 2019, *MNRAS*, 482, 5685
- Hamann, J., Covi, L., Melchiorri, A., & Slosar, A. 2007, *Phys. Rev. D*, 76, 023503
- Hamann, J. & Wons, J. 2022, *J. Cosmology Astropart. Phys.*, 2022, 036
- Hamilton, A. J. S. 1998, in *Astrophysics and Space Science Library*, Vol. 231, *The Evolving Universe*, ed. D. Hamilton, 185
- Hannestad, S., Haugbølle, T., Jarnhus, P. R., & Sloth, M. S. 2010, *J. Cosmology Astropart. Phys.*, 2010, 001
- Hawking, S. W., Moss, I. G., & Stewart, J. M. 1982, *Phys. Rev. D*, 26, 2681
- Hazra, D. K., Antony, A., & Shafieloo, A. 2022, *J. Cosmology Astropart. Phys.*, 2022, 063
- Hazra, D. K., Paoletti, D., Ballardini, M., et al. 2018, *J. Cosmology Astropart. Phys.*, 2018, 017
- Hazra, D. K., Shafieloo, A., Smoot, G. F., & Starobinsky, A. A. 2014a, *J. Cosmology Astropart. Phys.*, 2014, 048
- Hazra, D. K., Shafieloo, A., Smoot, G. F., & Starobinsky, A. A. 2016, *J. Cosmology Astropart. Phys.*, 2016, 009
- Hazra, D. K., Shafieloo, A., & Souradeep, T. 2014b, *J. Cosmology Astropart. Phys.*, 2014, 011
- Howlett, C., Manera, M., & Percival, W. J. 2015, *Astronomy and Computing*, 12, 109
- Hu, B. & Torrado, J. 2015, *Phys. Rev. D*, 91, 064039
- Huang, Z., Verde, L., & Vernizzi, F. 2012, *J. Cosmology Astropart. Phys.*, 2012, 005
- Kaiser, N. 1987, *MNRAS*, 227, 1
- Karagiannis, D., Lazanu, A., Liguori, M., et al. 2018, *MNRAS*, 478, 1341
- Karagiannis, D., Maartens, R., & Randrianjanahary, L. F. 2022, *J. Cosmology Astropart. Phys.*, 2022, 003
- Keeley, R. E., Shafieloo, A., Hazra, D. K., & Souradeep, T. 2020, *J. Cosmology Astropart. Phys.*, 2020, 055
- Knox, L. 1995, *Phys. Rev. D*, 52, 4307
- Laureijs, R., Amiaux, J., Arduini, S., et al. 2011, *arXiv e-prints*, arXiv:1110.3193
- Li, Y., Zhu, H.-M., & Li, B. 2022, *MNRAS*, 514, 4363
- Linde, A. D. 1982, *Physics Letters B*, 108, 389
- Linde, A. D. 1983, *Physics Letters B*, 129, 177
- LiteBIRD Collaboration: Allys, E., Arnold, K., Aumont, J., et al. 2023, *Progress of Theoretical and Experimental Physics*, 2023, 042F01
- Liu, M. & Huang, Z. 2020, *ApJ*, 897, 166
- Mao, T.-X., Wang, J., Li, B., et al. 2021, *MNRAS*, 501, 1499
- McDonald, P. & Roy, A. 2009, *J. Cosmology Astropart. Phys.*, 2009, 020
- McEwen, J. E., Fang, X., Hirata, C. M., & Blazek, J. A. 2016, *J. Cosmology Astropart. Phys.*, 2016, 015
- Mead, A. J., Heymans, C., Lombriser, L., et al. 2016, *MNRAS*, 459, 1468
- Meerburg, P. D., Münchmeyer, M., & Wandelt, B. 2016, *Phys. Rev. D*, 93, 043536
- Meerburg, P. D., Spergel, D. N., & Wandelt, B. D. 2014, *Phys. Rev. D*, 89, 063537
- Meerburg, P. D., Wijers, R. A. M. J., & van der Schaar, J. P. 2012, *MNRAS*, 421, 369
- Mergulhão, T., Beutler, F., & Peacock, J. A. 2023, *J. Cosmology Astropart. Phys.*, 2023, 012
- Miranda, V. & Hu, W. 2014, *Phys. Rev. D*, 89, 083529
- Miranda, V., Hu, W., & Dvorkin, C. 2015, *Phys. Rev. D*, 91, 063514
- Mohayaee, R., Frisch, U., Matarrese, S., & Sobolevskii, A. 2003, *A&A*, 406, 393
- Monaco, P. & Efstathiou, G. 1999, *MNRAS*, 308, 763
- Mortonson, M. J., Dvorkin, C., Peiris, H. V., & Hu, W. 2009, *Phys. Rev. D*, 79, 103519
- Mukhanov, V. F. & Chibisov, G. V. 1981, *Soviet Journal of Experimental and Theoretical Physics Letters*, 33, 532
- Mukherjee, P. & Wang, Y. 2003, *ApJ*, 599, 1
- Naik, S. S., Furuuchi, K., & Chingambam, P. 2022, *J. Cosmology Astropart. Phys.*, 2022, 016
- Nusser, A. & Branchini, E. 2000, *MNRAS*, 313, 587
- Okamoto, T. & Hu, W. 2003, *Phys. Rev. D*, 67, 083002
- Palma, G. A., Sapone, D., & Sypsas, S. 2018, *J. Cosmology Astropart. Phys.*, 2018, 004
- Peebles, P. J. E. 1989, *ApJ*, 344, L53
- Peiris, H. V., Komatsu, E., Verde, L., et al. 2003, *ApJS*, 148, 213
- Planck Collaboration: Ade, P. A. R., Aghanim, N., Armitage-Caplan, C., et al. 2014a, *A&A*, 571, A24
- Planck Collaboration: Ade, P. A. R., Aghanim, N., Armitage-Caplan, C., et al. 2014b, *A&A*, 571, A22
- Planck Collaboration: Ade, P. A. R., Aghanim, N., Arnaud, M., et al. 2016a, *A&A*, 594, A17
- Planck Collaboration: Ade, P. A. R., Aghanim, N., Arnaud, M., et al. 2016b, *A&A*, 594, A20
- Planck Collaboration: Aghanim, N., Akrami, Y., Arroja, F., et al. 2020a, *A&A*, 641, A1
- Planck Collaboration: Aghanim, N., Akrami, Y., Ashdown, M., et al. 2020b, *A&A*, 641, A6
- Planck Collaboration: Aghanim, N., Akrami, Y., Ashdown, M., et al. 2020c, *A&A*, 641, A5
- Planck Collaboration: Akrami, Y., Arroja, F., Ashdown, M., et al. 2020a, *A&A*, 641, A10
- Planck Collaboration: Akrami, Y., Arroja, F., Ashdown, M., et al. 2020b, *A&A*, 641, A9
- Sarpa, E., Schimd, C., Branchini, E., & Matarrese, S. 2019, *MNRAS*, 484, 3818
- Sato, K. 1981, *MNRAS*, 195, 467
- Schaap, W. E. & van de Weygaert, R. 2000, *A&A*, 363, L29
- Schmid, F. & Hui, L. 2013, *Physical Review Letters*, 110, 011301
- Schmidt, F. 2016, *Phys. Rev. D*, 93, 063512
- Schmidt, F. & Kamionkowski, M. 2010, *Phys. Rev. D*, 82, 103002
- Schmittfull, M., Baldauf, T., & Zaldarriaga, M. 2017, *Phys. Rev. D*, 96, 023505
- Scoccimarro, R., Hui, L., Manera, M., & Chan, K. C. 2012, *Phys. Rev. D*, 85, 083002
- Sefusatti, E., Vale, C., Kadota, K., & Frieman, J. 2007, *ApJ*, 658, 669
- Senatore, L. & Trevisan, G. 2018, *J. Cosmology Astropart. Phys.*, 2018, 019
- Shi, Y., Cautun, M., & Li, B. 2018, *Phys. Rev. D*, 97, 023505
- Slosar, A., Chen, X., Dvorkin, C., et al. 2019, *BAAS*, 51, 98
- Springel, V. 2005, *MNRAS*, 364, 1105
- Springel, V., White, S. D. M., Tormen, G., & Kauffmann, G. 2001, *MNRAS*, 328, 726
- Starobinsky, A. A. 1980, *Physics Letters B*, 91, 99
- Starobinsky, A. A. 1992, *Soviet Journal of Experimental and Theoretical Physics Letters*, 55, 489
- Tassev, S., Eisenstein, D. J., Wandelt, B. D., & Zaldarriaga, M. 2015, *arXiv e-prints*, arXiv:1502.07751
- Tassev, S., Zaldarriaga, M., & Eisenstein, D. J. 2013, *J. Cosmology Astropart. Phys.*, 2013, 036
- Teyssier, R. 2002, *A&A*, 385, 337
- Torrado, J., Hu, B., & Achúcarro, A. 2017, *Phys. Rev. D*, 96, 083515
- van de Weygaert, R. & Schaap, W. 2009, *The Cosmic Web: Geometric Analysis*, ed. V. J. Martínez, E. Saar, E. Martínez-González, & M. J. Pons-Bordería, Vol. 665, 291–413
- Vasudevan, A., Ivanov, M. M., Sibiryakov, S., & Lesgourgues, J. 2019, *J. Cosmology Astropart. Phys.*, 2019, 037
- Viel, M., Haehnelt, M. G., & Springel, V. 2010, *J. Cosmology Astropart. Phys.*, 2010, 015
- Villaescusa-Navarro, F., Naess, S., Genel, S., et al. 2018, *ApJ*, 867, 137
- Vlah, Z., Seljak, U., Yat Chu, M., & Feng, Y. 2016, *J. Cosmology Astropart. Phys.*, 2016, 057
- Wang, X., Yu, H.-R., Zhu, H.-M., et al. 2017, *ApJ*, 841, L29
- Wang, Y., Li, B., & Cautun, M. 2020, *MNRAS*, 497, 3451
- Wang, Y. & Mathews, G. J. 2002, *ApJ*, 573, 1
- Wang, Y., Spergel, D. N., & Strauss, M. A. 1999, *ApJ*, 510, 20

- Winther, H. A., Koyama, K., Manera, M., Wright, B. S., & Zhao, G.-B. 2017, *J. Cosmology Astropart. Phys.*, 2017, 006
- Wright, B. S., Winther, H. A., & Koyama, K. 2017, *J. Cosmology Astropart. Phys.*, 2017, 054
- Xu, Y., Hamann, J., & Chen, X. 2016, *Phys. Rev. D*, 94, 123518
- Zeng, C., Kovetz, E. D., Chen, X., et al. 2019, *Phys. Rev. D*, 99, 043517
- Zhan, H., Knox, L., Tyson, J. A., & Margoniner, V. 2006, *ApJ*, 640, 8
- Zhu, H.-M., Yu, Y., Pen, U.-L., Chen, X., & Yu, H.-R. 2017, *Phys. Rev. D*, 96, 123502
-
- ¹ Dipartimento di Fisica e Scienze della Terra, Università degli Studi di Ferrara, Via Giuseppe Saragat 1, 44122 Ferrara, Italy
- ² Istituto Nazionale di Fisica Nucleare, Sezione di Ferrara, Via Giuseppe Saragat 1, 44122 Ferrara, Italy
- ³ INAF-Osservatorio di Astrofisica e Scienza dello Spazio di Bologna, Via Piero Gobetti 93/3, 40129 Bologna, Italy
- ⁴ Instituto de Física Teórica UAM-CSIC, Campus de Cantoblanco, 28049 Madrid, Spain
- ⁵ CERCA/ISO, Department of Physics, Case Western Reserve University, 10900 Euclid Avenue, Cleveland, OH 44106, USA
- ⁶ INFN-Bologna, Via Irnerio 46, 40126 Bologna, Italy
- ⁷ Department of Physics and Astronomy, University of the Western Cape, Bellville, Cape Town, 7535, South Africa
- ⁸ Department of Physics, Institute for Computational Cosmology, Durham University, South Road, DH1 3LE, UK
- ⁹ Department of Physics & Astronomy, University of Sussex, Brighton BN1 9QH, UK
- ¹⁰ Université St Joseph; Faculty of Sciences, Beirut, Lebanon
- ¹¹ Institut de Recherche en Astrophysique et Planétologie (IRAP), Université de Toulouse, CNRS, UPS, CNES, 14 Av. Edouard Belin, 31400 Toulouse, France
- ¹² Institut für Theoretische Physik, University of Heidelberg, Philosophenweg 16, 69120 Heidelberg, Germany
- ¹³ Departamento de Física, FCFM, Universidad de Chile, Blanco Encalada 2008, Santiago, Chile
- ¹⁴ Institute Lorentz, Leiden University, PO Box 9506, Leiden 2300 RA, The Netherlands
- ¹⁵ Departamento de Física, Universidad del País Vasco UPV-EHU, 48940 Leioa, Spain
- ¹⁶ Dipartimento di Fisica e Astronomia, Università di Bologna, Via Gobetti 93/2, 40129 Bologna, Italy
- ¹⁷ INFN-Sezione di Bologna, Viale Berti Pichat 6/2, 40127 Bologna, Italy
- ¹⁸ Dipartimento di Fisica e Astronomia "G. Galilei", Università di Padova, Via Marzolo 8, 35131 Padova, Italy
- ¹⁹ INFN-Padova, Via Marzolo 8, 35131 Padova, Italy
- ²⁰ INAF-Osservatorio Astronomico di Padova, Via dell'Osservatorio 5, 35122 Padova, Italy
- ²¹ European Space Agency/ESTEC, Keplerlaan 1, 2201 AZ Noordwijk, The Netherlands
- ²² Institute for Theoretical Particle Physics and Cosmology (TTK), RWTH Aachen University, 52056 Aachen, Germany
- ²³ Gran Sasso Science Institute (GSSI), Viale F. Crispi 7, L'Aquila (AQ), 67100, Italy
- ²⁴ INFN – Laboratori Nazionali del Gran Sasso (LNGS), L'Aquila (AQ), 67100, Italy
- ²⁵ Institute of Theoretical Astrophysics, University of Oslo, P.O. Box 1029 Blindern, 0315 Oslo, Norway
- ²⁶ IFPU, Institute for Fundamental Physics of the Universe, via Beirut 2, 34151 Trieste, Italy
- ²⁷ INAF-Osservatorio Astronomico di Trieste, Via G. B. Tiepolo 11, 34143 Trieste, Italy
- ²⁸ SISSA, International School for Advanced Studies, Via Bonomea 265, 34136 Trieste TS, Italy
- ²⁹ INFN, Sezione di Trieste, Via Valerio 2, 34127 Trieste TS, Italy
- ³⁰ Department of Astronomy, Stockholm University, Albanova, 10691 Stockholm, Sweden
- ³¹ Institut d'Astrophysique de Paris, 98bis Boulevard Arago, 75014, Paris, France
- ³² Institut d'Astrophysique de Paris, UMR 7095, CNRS, and Sorbonne Université, 98 bis boulevard Arago, 75014 Paris, France
- ³³ The Institute of Mathematical Sciences, HBNI, CIT Campus, Chennai, 600113, India
- ³⁴ Homi Bhabha National Institute, Training School Complex, Anushakti Nagar, Mumbai 400085, India
- ³⁵ Department of Physics, P.O. Box 64, 00014 University of Helsinki, Finland
- ³⁶ Helsinki Institute of Physics, Gustaf Hällströmin katu 2, University of Helsinki, Helsinki, Finland
- ³⁷ Institute of Cosmology and Gravitation, University of Portsmouth, Portsmouth PO1 3FX, UK
- ³⁸ INAF-Osservatorio Astronomico di Brera, Via Brera 28, 20122 Milano, Italy
- ³⁹ INAF-Osservatorio Astrofisico di Torino, Via Osservatorio 20, 10025 Pino Torinese (TO), Italy
- ⁴⁰ Dipartimento di Fisica, Università di Genova, Via Dodecaneso 33, 16146, Genova, Italy
- ⁴¹ INFN-Sezione di Genova, Via Dodecaneso 33, 16146, Genova, Italy
- ⁴² Department of Physics "E. Pancini", University Federico II, Via Cinthia 6, 80126, Napoli, Italy
- ⁴³ INAF-Osservatorio Astronomico di Capodimonte, Via Moiariello 16, 80131 Napoli, Italy
- ⁴⁴ INFN section of Naples, Via Cinthia 6, 80126, Napoli, Italy
- ⁴⁵ Instituto de Astrofísica e Ciências do Espaço, Universidade do Porto, CAUP, Rua das Estrelas, PT4150-762 Porto, Portugal
- ⁴⁶ Dipartimento di Fisica, Università degli Studi di Torino, Via P. Giuria 1, 10125 Torino, Italy
- ⁴⁷ INFN-Sezione di Torino, Via P. Giuria 1, 10125 Torino, Italy
- ⁴⁸ INAF-IASF Milano, Via Alfonso Corti 12, 20133 Milano, Italy
- ⁴⁹ Institut de Física d'Altes Energies (IFAE), The Barcelona Institute of Science and Technology, Campus UAB, 08193 Bellaterra (Barcelona), Spain
- ⁵⁰ Port d'Informació Científica, Campus UAB, C. Albareda s/n, 08193 Bellaterra (Barcelona), Spain
- ⁵¹ INAF-Osservatorio Astronomico di Roma, Via Frascati 33, 00078 Monteporzio Catone, Italy
- ⁵² Dipartimento di Fisica e Astronomia "Augusto Righi" - Alma Mater Studiorum Università di Bologna, Viale Berti Pichat 6/2, 40127 Bologna, Italy
- ⁵³ Institute for Astronomy, University of Edinburgh, Royal Observatory, Blackford Hill, Edinburgh EH9 3HJ, UK
- ⁵⁴ European Space Agency/ESRIN, Largo Galileo Galilei 1, 00044 Frascati, Roma, Italy
- ⁵⁵ ESAC/ESA, Camino Bajo del Castillo, s/n., Urb. Villafraanca del Castillo, 28692 Villanueva de la Cañada, Madrid, Spain
- ⁵⁶ University of Lyon, Univ Claude Bernard Lyon 1, CNRS/IN2P3, IP2I Lyon, UMR 5822, 69622 Villeurbanne, France
- ⁵⁷ Institute of Physics, Laboratory of Astrophysics, Ecole Polytechnique Fédérale de Lausanne (EPFL), Observatoire de Sauverny, 1290 Versoix, Switzerland
- ⁵⁸ UCB Lyon 1, CNRS/IN2P3, IUF, IP2I Lyon, 4 rue Enrico Fermi, 69622 Villeurbanne, France
- ⁵⁹ Departamento de Física, Faculdade de Ciências, Universidade de Lisboa, Edifício C8, Campo Grande, PT1749-016 Lisboa, Portugal
- ⁶⁰ Instituto de Astrofísica e Ciências do Espaço, Faculdade de Ciências, Universidade de Lisboa, Campo Grande, 1749-016 Lisboa, Portugal
- ⁶¹ Department of Astronomy, University of Geneva, ch. d'Ecogia 16, 1290 Versoix, Switzerland
- ⁶² INAF-Istituto di Astrofisica e Planetologia Spaziali, via del Fosso del Cavaliere, 100, 00100 Roma, Italy
- ⁶³ Université Paris-Saclay, Université Paris Cité, CEA, CNRS, AIM, 91191, Gif-sur-Yvette, France
- ⁶⁴ Max Planck Institute for Extraterrestrial Physics, Giessenbachstr. 1, 85748 Garching, Germany
- ⁶⁵ University Observatory, Faculty of Physics, Ludwig-Maximilians-Universität, Scheinerstr. 1, 81679 Munich, Germany
- ⁶⁶ Jet Propulsion Laboratory, California Institute of Technology, 4800 Oak Grove Drive, Pasadena, CA, 91109, USA
- ⁶⁷ von Hoerner & Sulger GmbH, Schloßplatz 8, 68723 Schwetzingen, Germany

- ⁶⁸ Technical University of Denmark, Elektrovej 327, 2800 Kgs. Lyngby, Denmark
- ⁶⁹ Cosmic Dawn Center (DAWN), Denmark
- ⁷⁰ Max-Planck-Institut für Astronomie, Königstuhl 17, 69117 Heidelberg, Germany
- ⁷¹ Aix-Marseille Université, CNRS/IN2P3, CPPM, Marseille, France
- ⁷² Université de Genève, Département de Physique Théorique and Centre for Astroparticle Physics, 24 quai Ernest-Ansermet, CH-1211 Genève 4, Switzerland
- ⁷³ NOVA optical infrared instrumentation group at ASTRON, Oude Hoogeveensedijk 4, 7991PD, Dwingeloo, The Netherlands
- ⁷⁴ Universität Bonn, Argelander-Institut für Astronomie, Auf dem Hügel 71, 53121 Bonn, Germany
- ⁷⁵ Aix-Marseille Université, CNRS, CNES, LAM, Marseille, France
- ⁷⁶ Dipartimento di Fisica e Astronomia "Augusto Righi" - Alma Mater Studiorum Università di Bologna, via Piero Gobetti 93/2, 40129 Bologna, Italy
- ⁷⁷ Université Paris Cité, CNRS, Astroparticule et Cosmologie, 75013 Paris, France
- ⁷⁸ Department of Physics and Astronomy, University of Aarhus, Ny Munkegade 120, DK-8000 Aarhus C, Denmark
- ⁷⁹ Centre for Astrophysics, University of Waterloo, Waterloo, Ontario N2L 3G1, Canada
- ⁸⁰ Department of Physics and Astronomy, University of Waterloo, Waterloo, Ontario N2L 3G1, Canada
- ⁸¹ Perimeter Institute for Theoretical Physics, Waterloo, Ontario N2L 2Y5, Canada
- ⁸² Université Paris-Saclay, Université Paris Cité, CEA, CNRS, Astrophysique, Instrumentation et Modélisation Paris-Saclay, 91191 Gif-sur-Yvette, France
- ⁸³ Space Science Data Center, Italian Space Agency, via del Politecnico snc, 00133 Roma, Italy
- ⁸⁴ Centre National d'Etudes Spatiales – Centre spatial de Toulouse, 18 avenue Edouard Belin, 31401 Toulouse Cedex 9, France
- ⁸⁵ Institute of Space Science, Str. Atomistilor, nr. 409 Măgurele, Ilfov, 077125, Romania
- ⁸⁶ Universitäts-Sternwarte München, Fakultät für Physik, Ludwig-Maximilians-Universität München, Scheinerstrasse 1, 81679 München, Germany
- ⁸⁷ Universität Innsbruck, Institut für Astro- und Teilchenphysik, Technikerstr. 25/8, 6020 Innsbruck, Austria
- ⁸⁸ Institut d'Estudis Espacials de Catalunya (IEEC), Carrer Gran Capitá 2-4, 08034 Barcelona, Spain
- ⁸⁹ Institute of Space Sciences (ICE, CSIC), Campus UAB, Carrer de Can Magrans, s/n, 08193 Barcelona, Spain
- ⁹⁰ Satlantis, University Science Park, Sede Bld 48940, Leioa-Bilbao, Spain
- ⁹¹ AIM, CEA, CNRS, Université Paris-Saclay, Université de Paris, 91191 Gif-sur-Yvette, France
- ⁹² Centro de Investigaciones Energéticas, Medioambientales y Tecnológicas (CIEMAT), Avenida Complutense 40, 28040 Madrid, Spain
- ⁹³ Instituto de Astrofísica e Ciências do Espaço, Faculdade de Ciências, Universidade de Lisboa, Tapada da Ajuda, 1349-018 Lisboa, Portugal
- ⁹⁴ Universidad Politécnica de Cartagena, Departamento de Electrónica y Tecnología de Computadoras, Plaza del Hospital 1, 30202 Cartagena, Spain
- ⁹⁵ Kapteyn Astronomical Institute, University of Groningen, PO Box 800, 9700 AV Groningen, The Netherlands
- ⁹⁶ Infrared Processing and Analysis Center, California Institute of Technology, Pasadena, CA 91125, USA
- ⁹⁷ Junia, EPA department, 41 Bd Vauban, 59800 Lille, France

Appendix A: Comparison with dark matter N-body simulations

In Figs. A.1 and A.2, we compare the ratio between the matter power spectrum with primordial oscillations to the one obtained with a power-law PPS at redshift $z = 0$. We show analytic results obtained with PT at LO (blue) and NLO (orange) versus linear theory predictions (grey) and the nonlinear results obtained from N-body simulations (green).

Appendix B: Nonlinear reconstruction results

In Fig. B.1, we compare the wiggle $O_w(k)$, which is the ratio between the wiggled and no-wiggle $P(k)$, for all 20 wiggled models: linear models in the first two rows and logarithmic models in the bottom two rows as shown by the legend. The four subpanels of each row, from bottom to top, are the results for $z = 1.5, 1.0, 0.5$, and 0. Linear theory predictions (which in practice are replaced by the measured $P(k)$ from the initial condition snapshots at $z = 9$) are shown by black solid curves, while the measurements from the fully nonlinear and reconstructed matter density fields are shown by blue solid and orange dashed curves.

Structure formation greatly damps the wiggles, and this impact is strongest for the low-frequency wiggle models, given that there are fewer peaks in the k range shown. The extreme example is $\omega_{\log} = 10^{0.2}$, for which at $z < 1$ the only peak in the entire k range shown here is completely invisible. Reconstruction is expected to be useful here, as shown by the orange curves in the corresponding panels. Even for models with very high wiggle frequencies, such as $\omega_{\log} = 10^2$, the wiggles can be well reconstructed down to $k \simeq 1 h \text{Mpc}^{-1}$.

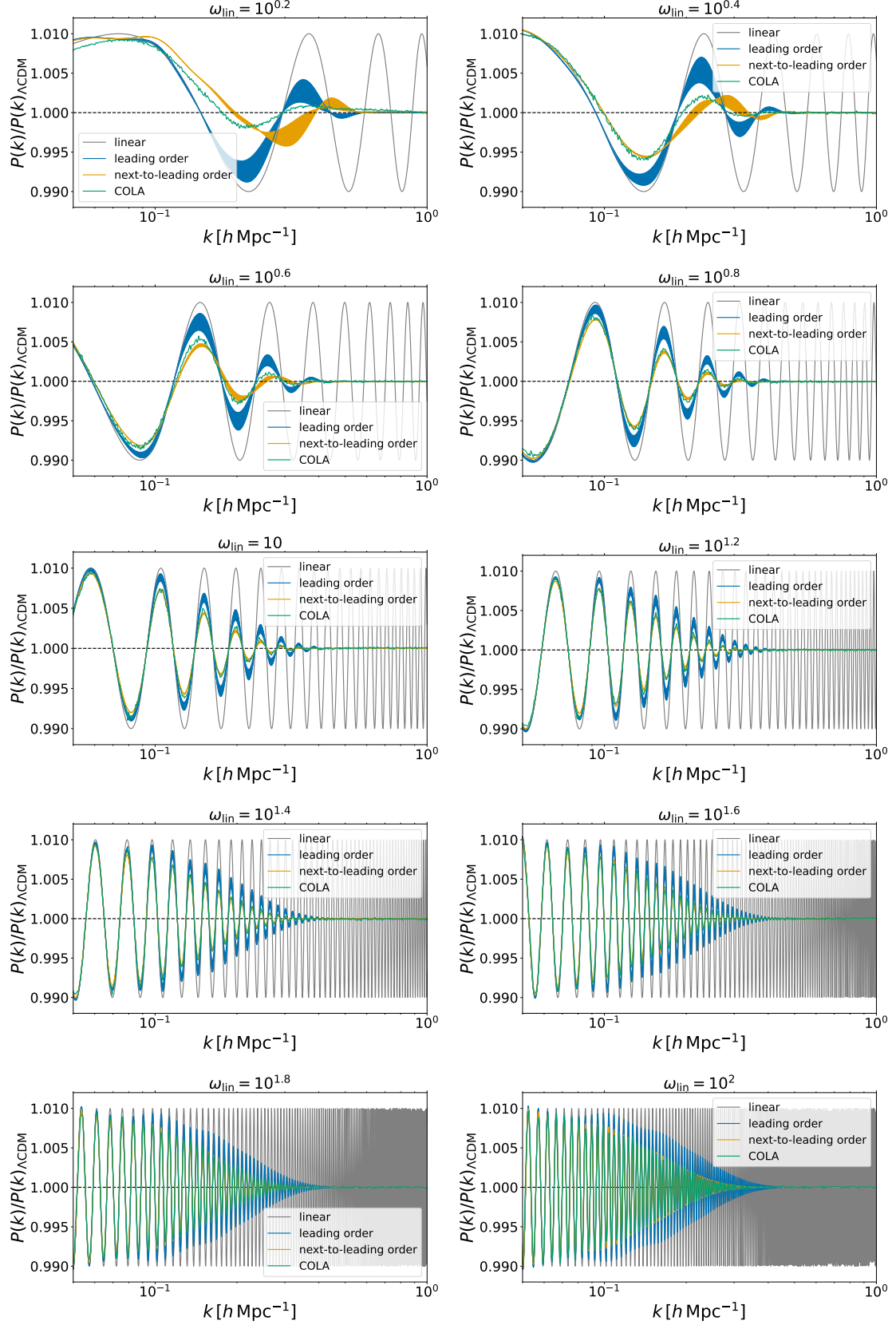


Fig. A.1. Ratio of IR resummed matter power spectrum at LO (blue) and NLO (orange) obtained for the linear oscillations to the one obtained with a power-law PPS at redshift $z = 0$ varying the IR separation scale $k_s = \epsilon k$ with $\epsilon \in (0.3, 0.7)$. Also shown are the linear results (grey) and the ones obtained from N-body simulations (green).

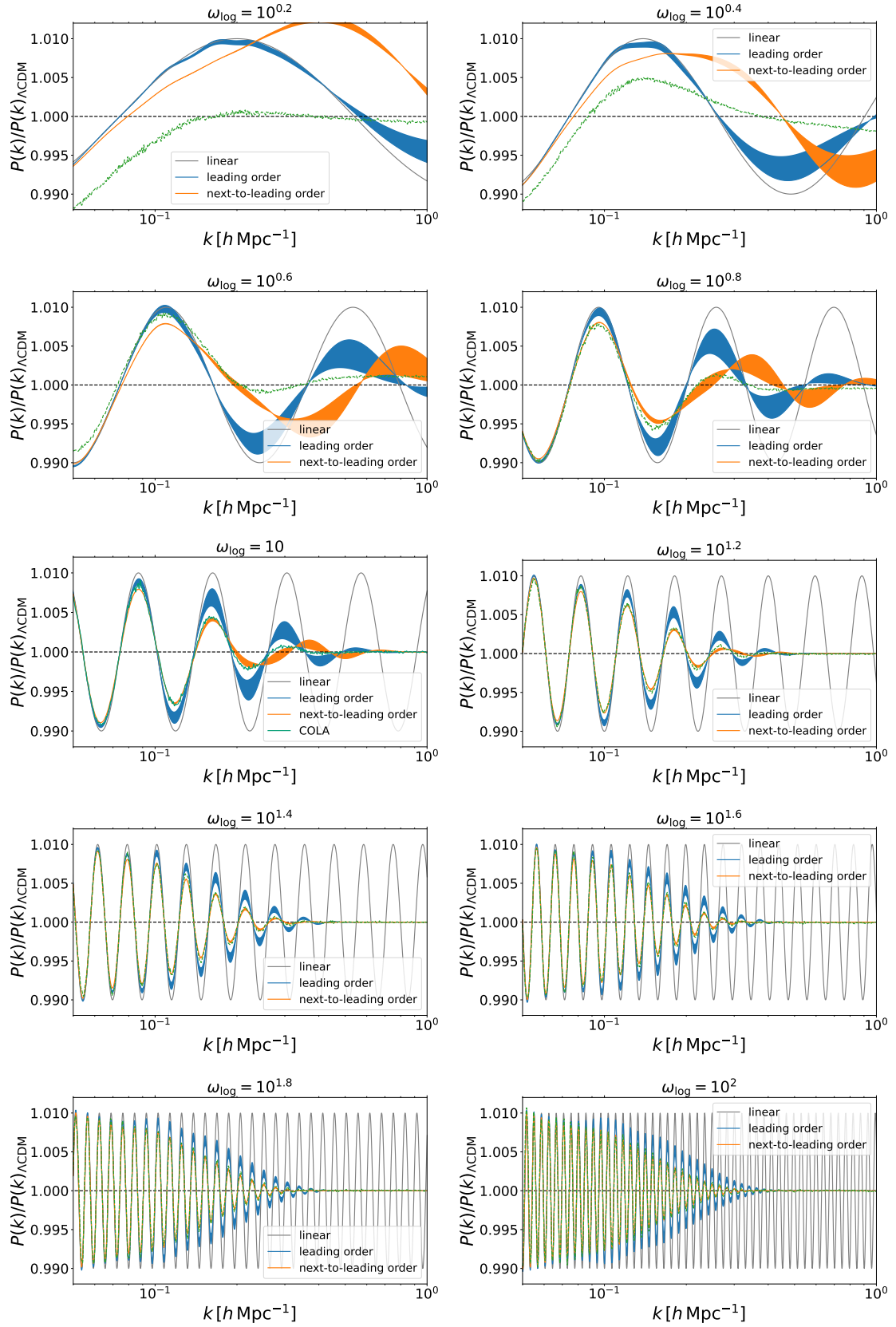


Fig. A.2. As in Fig. A.1, but for the logarithmic oscillations.

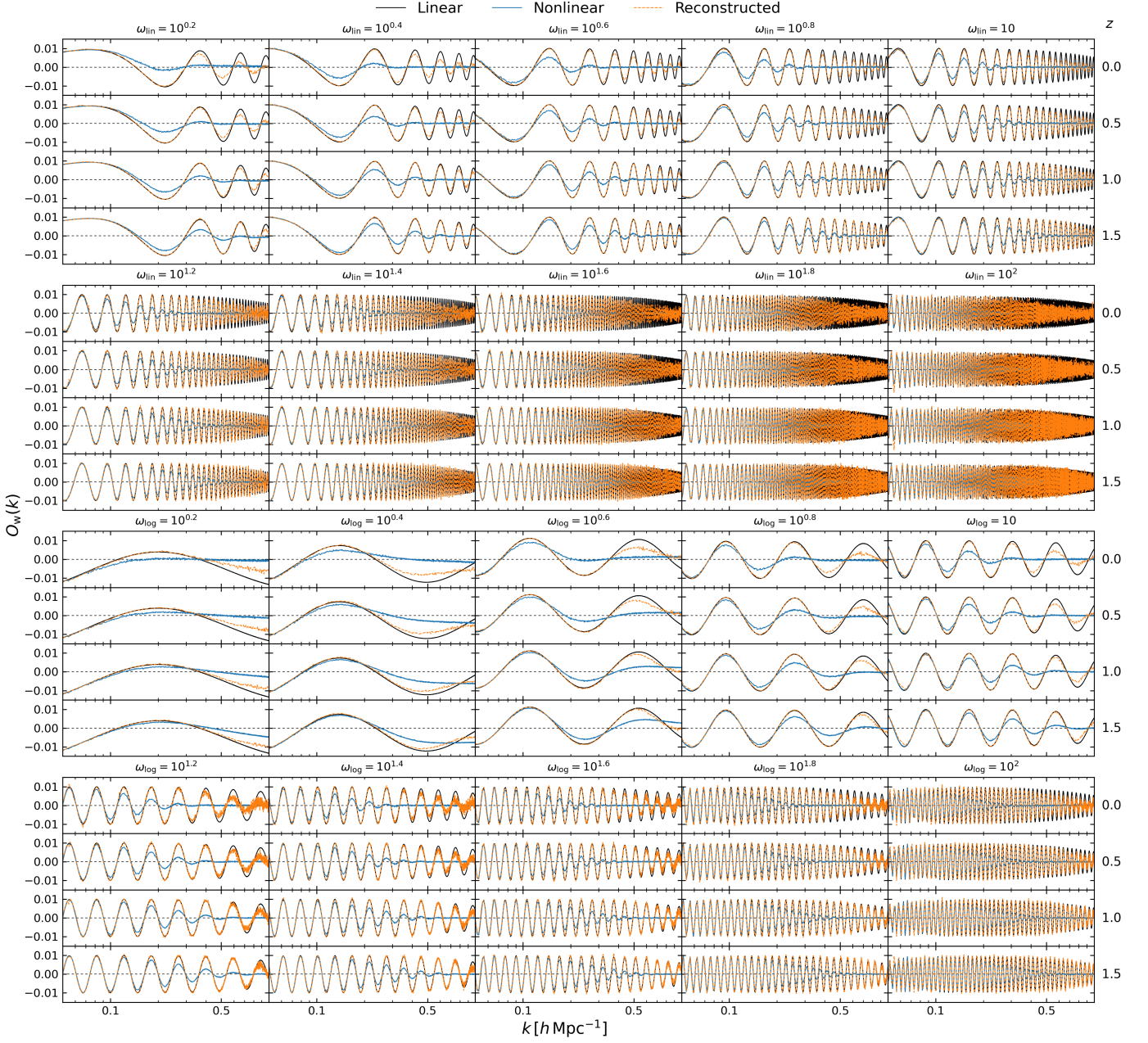


Fig. B.1. Ratio of the linear (black solid curves), nonlinear (blue solid curves), and reconstructed (orange dashed curves) density fields for the 20 selected feature models to the one obtained with a power-law PPS. Each of the rows is respectively for the redshifts marked on the right. The linear $O_w(k)$ are measured from the initial conditions at $z = 9$, the nonlinear $O_w(k)$ are from the output snapshots of DM, and the reconstructed $O_w(k)$ are from the reconstructed density fields.